Wesleyan University The Honors College

Unseen Worlds: A Search for Exoplanet Transits of Bright Early-Type Stars

by

Cassidy Miles Egan Soloff
Class of 2022

A thesis submitted to the
faculty of Wesleyan University
in partial fulfillment of the requirements for the
Degree of Bachelor of Arts
with Departmental Honors in Astronomy

Middletown, Connecticut April, 2022

"From imperfection's murkiest cloud,

Darts always forth one ray of perfect light,

One flash of Heaven's glory."

–Walt Whitman, Leaves Of Grass

Acknowledgments

Thank you to my advisor Seth Redfield who introduced me academically to the field of Astronomy my freshmen year when I took Introduction to Astronomy. His enthusiasm and passion as a professor motivated me to join his research group the following year and eventually pursue a lifelong career in research. Thank you for your unrelenting support of me from the moment I arrived at Wesleyan and through the struggles of the pandemic. Thank you for fostering the curiosity that has driven my love for research. Through your role as a professor, advisor and mentor, I have learned more than I could have ever imagined and have become the scientist I always wanted to be.

Thank you Roy Kilgard for teaching me the technical skills that have been fundamental for my conducting research. Through both Observational Astronomy and the countless hours spent working through telescope issues, I have become a better coder, observer and researcher. Thank you Meredith Hughes for making me a better researcher and teacher. Collecting and analyzing radio data taught me so many valuable skills that proved vital to this project. Thank you to Ed Moran for being a great professor and academic advisor. Your instruction for Galaxies, Quasars, & Cosmology has driven a new excitement in fields of astronomy that were less familiar to me.

Thank you to the Van Vleck Observatory community for creating such a sup-

portive and collaborative environment. Thank you Kyle McGregor for working with me on the telescope and making long nights of observation and troubleshooting so much fun! Thank you to my fellow Astronomy seniors Ben Rubel and Jack Root for being such great housemates, band members, study buddies and friends. Thank you to the Wesleyan Astronomy Club, its founding fathers Ben Martinez and Gil Garcia, and prime minister Aidan Jones.

Thank you to my family for supporting me my whole life and through the challenges of these past four years. Thank you to my mom for providing the wisdom to overcome my most difficult obstacles. Thank you to my brother Zef for supporting and engaging in my scientific and artistic passions. Thank you Jasper for all the laughter and joy you spread.

We acknowledge the support for this project through the Wesleyan University Summer Research Fellowship and the Undergraduate Research Grant awarded by the NASA Connecticut Space Grant Consortium. This research has made use of the NASA Exoplanet Archive, which is operated by the California Institute of Technology, under contract with the National Aeronautics and Space Administration under the Exoplanet Exploration Program.

Contents

Chapter 1

Introduction

As astronomers have continued to search the universe for other worlds, it has become increasingly apparent how prevalent they are. Today, astronomers believe that nearly every star has at least one exoplanet (Cassan et al. 2012). By studying these extrasolar planets, called exoplanets, we have not only seen planets similar to those in our solar system but ones with extraordinary conditions and that orbit stars very different than our own. We see water worlds like GJ 1214 b (Charbonneau et al. 2009), lava worlds like CoRoT-7b (Léger et al. 2009), hot Jupiter-sized planets completing full orbits in less than a week like 51 Pegasi b (Mayor & Queloz 1995), giant planets with orbits of 27,000 years like CVSO 30 b (Schmidt et al. 2016), diamond planets like 55 Cancri e (Madhusudhan et al. 2012), tightly packed system like the 7 planet TRAPPIST-1 system (Gillon et al. 2017), planets around white dwarfs like WD J0914+1914 b (Gänsicke et al. 2019) and neutron stars like the PSR1257 + 12 system (Wolszczan & Frail 1992). To make these discoveries, we are only limited by our technology and the time we are willing to commit to searching. With the arrival of Wesleyan's 24-inch, automated research telescope, we have the ability to search for exoplanets around stars where other surveys struggle to take observations. The two predominant methods for detection, radial velocity and wide-field transit surveys, face challenges in detecting early-type and bright stars respectively. To expand the diversity of planetary systems, we design

an exoplanet survey that searches this underrepresented sample.

1.1 Exoplanet Detections

The study of exoplanetary systems gives us the unique ability to investigate worlds much different from our own while strengthening our understanding of the common processes that lead to the formation of planets, atmospheres and the emergence of life. Searching for exoplanets around a diversity of stars broadens our knowledge of the environmental factors that shape the evolution and properties of exoplanets. As our technological abilities advance, the wealth of detections and the ability to categorize exoplanet properties has expanded dramatically.

There are many methods for detecting exoplanets. Pulsar timing led to the discovery of the first exoplanets and relies on detecting variations in the arrival of electromagnetic pulses from a neutron star to detect the gravitational influence of a planet (Wolszczan & Frail 1992). The transit method, which is described in Section 1.2.2, can determine the timing and duration of a planet passing in front of a star due to the planet obscuring some of the starlight. Transit timing variation uses the differences in transit times caused by the gravitational influence of other planets (Ballard et al. 2011). Transit duration variation can detect similar gravitation effects that change the duration of transits (Welsh et al. 2014). Gravitational microlensing relies on how General Relativity describes light bending around massive objects. When a closer star passes in front of a background star, the gravitational influence of the star can magnify the light from a distant star and detect the gravitational influence of an exoplanet orbiting the distant star (Beaulieu et al. 2006). Planets can even be imaged directly. Direct imaging of exoplanets requires a very powerful telescope and coronagraphs to block the light

from the host star. Large planets that orbit at great distances from their host star are detected most effectively (Macintosh et al. 2015). There are other methods of exoplanet detection but the vast majority are made using the radial velocity and transit techniques which I discuss in Sections 1.2.1 and 1.2.2 respectively.

According to the NASA Exoplanet Archive[1] as of 2022 Mar 18, there have been 4,521 exoplanet discoveries. Much of these discoveries are dominated by the *Kepler* mission which made 2402 discoveries released in 2014 and 2016 (Borucki et al. 2010). *Kepler* made use of the transit method (see Sec. 1.2.2) of exoplanet detection which accounts for 75.6% of all exoplanet detections while the remaining discoveries are dominated by the radial velocity method (19.4%; see Sec. 1.2.1). Both these methods have limitations in the types of stars they can effectively observe, especially in wide-field surveys. Using these deficiencies in the predominant methods of exoplanet detection, we craft an exoplanet detection campaign that will observe bright, early-type stars where transit surveys and the radial velocity methods struggle to make detections.

1.2 Detection Methods

1.2.1 Radial Velocity

The radial velocity method of exoplanet detection takes advantage of the fact that all bodies in a stellar system orbit around a common center of mass, including planets as well as the host star. In a single planet system, a star will complete a full orbit around the center of mass in the same time it takes the planet to orbit the center of mass. The star's orbit will be smaller than the planets because the center of mass location is weighted towards the more massive object. The star will

[1] https://exoplanetarchive.ipac.caltech.edu

have a velocity in the opposite direction reduced by the ratio of the star to planet mass. If any of this velocity is radial to an observer, it can be detected through the Doppler shift in a star's spectrum. Stellar radiation from a source moving towards the observer will be blueshifted and redshifted when moving away from the observer. The length of time it takes for the spectrum to return to the same Doppler shift with respect to the rest frequency of the star is the same as the period of the planet's orbit. When there is a multi-planet system, the individual contributions in Dopplers shifts of the host star's spectrum must be separated.

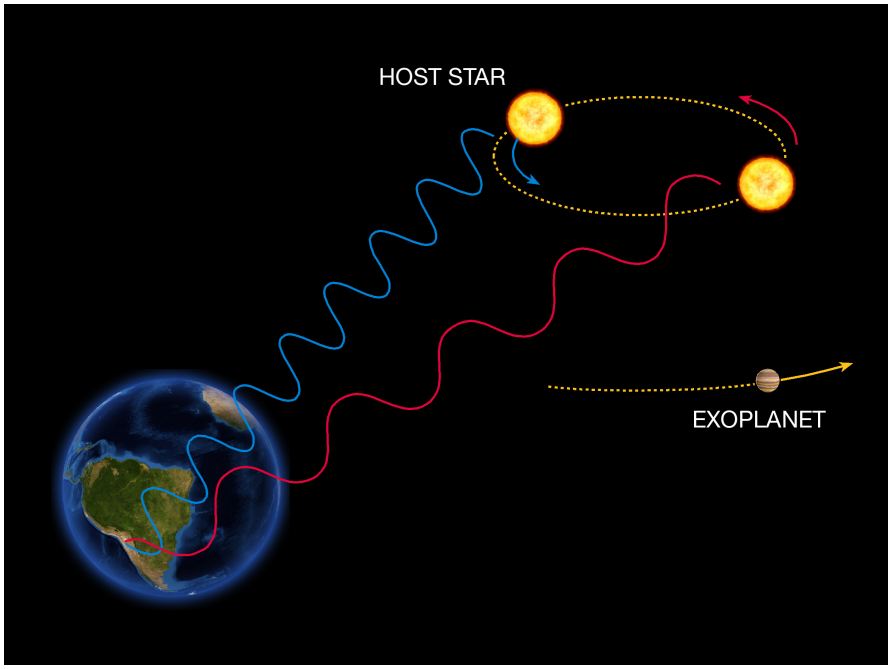

Figure 1.1: This diagram shows an exoplanet orbiting a single star. The star is shown in two positions: the leftward position in which the star is moving towards the Earth, causing the star's spectrum to be blueshifted and the rightward position where the star is moving away from the observer, causing the spectrum of the star to be redshifted. If this is a single planet system, the position of the planets is on the opposite side of the center of mass of the system. Source: European Southern Observatory

These radial velocity shifts are measured by viewing the spectrum of a star and seeing where absorption features shift in wavelength over time. These measurements produce a sinusoidal pattern that is influenced by factors such as the

inclination of the orbit, the eccentricity of the orbit and if multiple orbiting bodies are present. The amplitude of this Doppler shift is described by the radial velocity semi-amplitude K and is related to key properties of a planet's mass and orbit:

$$K = \sqrt{\frac{G}{1-e^2}} m_2 \sin i (m_1 + m_2)^{-1/2} a^{-1/2} \tag{1.1}$$

where G is the gravitational constant, e is the eccentricity of the planet's orbit, m_1 is the stellar mass, m_2 is the planetary mass and a is the semi-major axis of the planet.

Less massive stars with massive planets orbiting at close distances produce the greatest radial velocity semi-amplitude. Hotter stars are more massive, increasing the value of m_1 and decreasing K, thereby making it harder to detect an exoplanet. But the precision derived from radial velocity measurements also depends on the brightness of the star and its spectrum. Bright stars improve the signal to noise of spectral measurements but early-type stars have a more continuous spectrum for reasons outlined in Section 1.3. Doppler shifts are harder to measure for continuous spectrums.

1.2.2 Transit Method

The transit method of exoplanet discovery uses the observation of a transit to detect exoplanets by measuring a star's apparent flux over time. If the inclination of the planetary system is near 90 degrees, a primary transit occurs when the planet passes directly in front of the star it is orbiting, causing a temporary drop in flux. Secondary transit occurs when a planet passes behind the star, reducing the total flux of the star and planet because there is no longer a contribution of flux from starlight bouncing off the planet. For the transit method, primary

transits are used to detect planets because directly blocking starlight causes a greater drop in flux than secondary transits. For example, the secondary eclipse of the 0.081 Jupiter-mass planet HAT-P-11 b had a primary transit depth of 3429 ppm but a secondary transit depth of just 6.09 ppm (Huber et al. 2017).

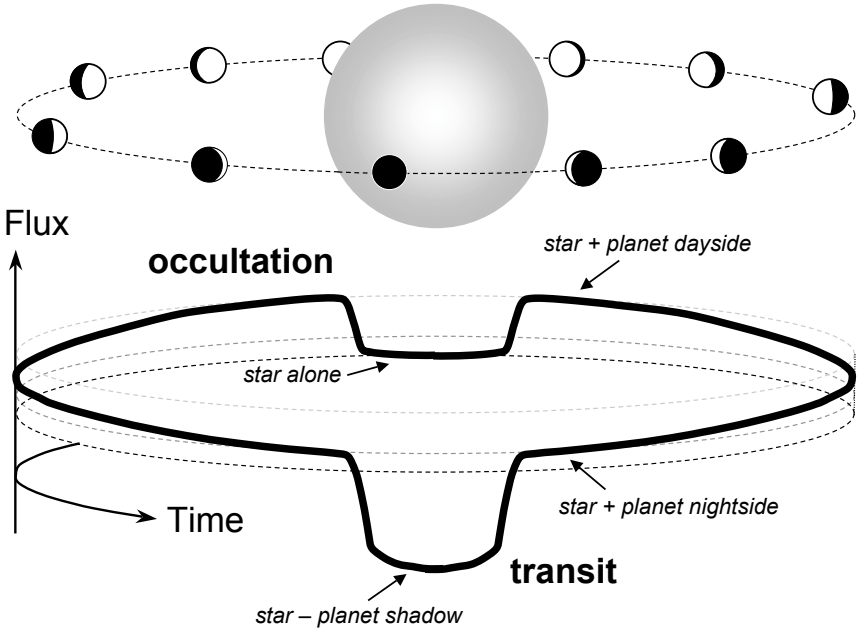

Figure 1.2: The apparent flux of the star is shown for different orientations of the planet. The primary transit yields the deepest drop in flux while the secondary transit, where the star occults the planet, produces a shallower drop in flux. Source: Winn (2010)

The primary parameter derived by the transit method is the radius of the planet (R_p) in terms of the radius of the host star (R_*). The depth of the drop in flux called the transit depth δ is given by:

$$\delta = \left(\frac{R_p}{R_*}\right)^2. \tag{1.2}$$

Equation 1.2 demonstrates the main bias of the transit method. Detections are easier for large planets around small stars. Despite the fact that stellar radius

increases with temperature, detections of planets around hot stars have been successfully made via the transit method. However, the context in which we used the transit method for detections is in wide-field surveys where many stars are observed for each exposure. Because a limited number of stars are close and luminous enough to appear bright, there are far fewer bright stars than dim stars. For this reason, transit surveys expose for dimmer stars because detections are more likely to be made with more targets visible.

Meanwhile, the dynamic range of wide-field transit surveys is insufficient at exposing for bright stars concurrently, leaving them saturated. Bright stars have enormous potential for follow-up studies because an enhanced flux will produce a high signal-to-noise. Better transmission spectroscopy can be obtained from bright stars. Transmission spectroscopy is conducted by comparing in and out of transit spectrums of a planetary system to find chemical features of the planetary atmosphere (Madhusudhan 2019) and even surface composition (Yu et al. 2021). Another spectroscopic effect that will be aided by bright stars is the Rossiter-McLaughlin effect where the blocking of light along the stellar surface affects the Doppler shifts in the star's spectrum due to the rotation of the star (Boué et al. 2013). As will be discussed in Section 2.1.3, many of the stars that will be used for this survey will have higher measured rotational speeds. By using the Rossiter-McLaughlin effect, we can reduce the uncertainty in rotational speed caused by ambiguity in the orientation of stellar systems. With a discovery of a bright early-type star, we can study hotter stellar systems in better detail.

Looking at Figure 1.3, we see the effects of the biases present in the transit and radial velocity methods by examining the temperature and magnitude of all stars with confirmed exoplanets. The transit method occupies the high magnitude section of the plot, with a concentration of detections for lower temperature planets

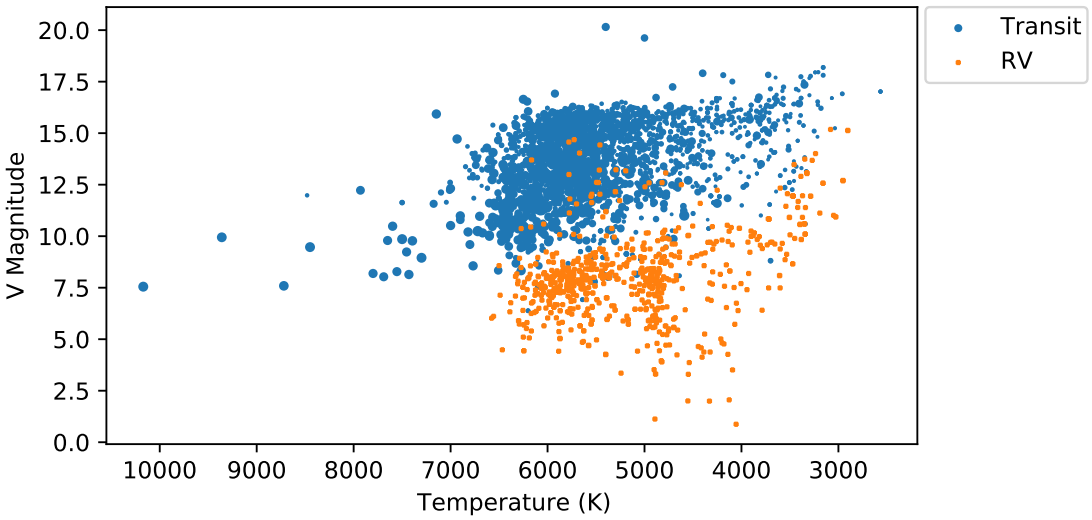

Figure 1.3: Stellar temperature effective and V magnitude of confirmed exoplanet detections by detection method. The transit method maker sizes are proportional to the planetary radius. Source: NASA Exoplanet Archive

where the radius of the star is smaller, making deeper exoplanet transit depths. There is a spattering of transit detections for high-temperature stars. The size of the dots for the transit method is proportional to the largest planet's radius in each stellar system. For these transit detections around these high-temperature stars, most of the planets have higher radii than the low stellar temperature detections because hot stars have larger radii and therefore require a larger planet size to make a detection.

The radial velocity detections occupy a distinct region of this plot: the bright and cool lower right corner. Beyond about 6,500 K, there is a lack of radial velocity detections because stellar spectra with many deep absorption lines cannot be obtained for hot stars as shown in Section 1.3.1. The stars detected by the radial velocity method are bright because these stars provide enough signal for spectroscopy. From this plot, we see exactly where we must focus this search. For temperatures greater than 6,500 K and magnitudes less than 8, there is a glaring

deficiency in detections. Next, I will examine the properties of these hot stars so we can better understand how we can make a detection and sources of variability that may be present in these stars.

1.3 Stellar Properties

As we have seen in Section 1.2.2, making a detection of a transiting planet is highly dependent on the properties of the host star. Therefore, of the sample of stars that are brighter and hotter than the stars where planets have been discovered, I shall examine what stellar features will maximize the likelihood of detection.

The temperature of a star on the main sequence provides us with the key information on the mass, radius and spectrum of a star. When a star is on the main sequence, it has contracted to a point where the pressure is high enough for nuclear fusion to take place in the core of the star. The Hertzsprung–Russell (HR) diagram plots stars in terms of temperature and luminosity. The curve on the HR diagram where stars powered by fusion fall is the main sequence.

Stars that appear to the left of the HR diagram are hotter stars that have shorter life spans because they radiate their energy at a faster rate than cooler stars. It was mistakenly thought that stars evolved from hot to cool, so hot stars are referred to as early-type stars. Similarly, cool stars are called late-type stars. In this thesis, I refer to hot or early-type stars as stars hotter than type G (the spectral type of the Sun) which includes O, B, A and F stars. This corresponds to effective temperatures hotter than 6,000 K.

Hot stars have distinct features that make it more difficult to detect their exoplanets. For one, their spectrums have fewer sharp absorption features than

cooler stars, making radial velocity measurements more difficult. Higher temperatures mean there are fewer non-ionized elements in the stellar atmosphere because the stellar radiation is more intense. Transitions between bound energy levels (bound-bound transitions) produce distinct absorption lines rather than continuous absorption features produced by ionization, free election transitions and electron scattering. The only dominant bound-bound transition lines still present in early-type stars are the hydrogen lines. However, it is difficult to make precise radial velocity using these few absorption features.

Even the fewer bound-bound transitions present in hot stars become obscured by modes of scattering predominant in hot stars. Collision de-excitation broadening, called Van der Waals broadening, happens when neutral atoms of the same species collide, splitting and shifting the energy level of the transition. The split energy levels cannot be resolved but cause a broadening to take place. These processes are more common in the conditions of early-type stellar atmospheres. The higher temperatures also produce greater levels of Doppler broadening, which causes absorption features to take a wider absorption profile.

The rotation of the star adds further broadening because of the radial motion of particles towards and away from the observer, blue and red shifting spectral lines. Early-type stars have considerably higher levels of rotation due to their short life span (Tassoul 2000). As stars age, they lose their angular momentum due to interactions with the material surrounding the star. Skumanich's Law empirically derives this relationship with rotation by relating the rotational velocity in km s^{-1} to age: $v \sin i = 5/\sqrt{\text{Age [Gyr]}}$. There also exists a $\sin i$ term in this equation because the inclination of a star is difficult to measure but still affects the rotational velocity we observe. However, stars with high $v \sin i$ are more likely to have inclinations closer to 90 degrees, meaning orbiting bodies will be more

likely to transit because $\sin 90° = 1$. There is, however, a trade-off between high a $v \sin i$ and transit detections because faster rotating stars may have more planets misaligned with the stellar plane of rotation (Albrecht et al. 2021).

The mass and radius of stars increase with temperature, but the mass increases more rapidly with temperature than radius because mass depends on the volume of a star which has an R_*^3 dependence. F and A-type stars have a range in radius from 1.15–1.8 $R_\odot$ while hotter, B and O-type stars range from 1.8 to above 6.6 $R_\odot$. The larger radius of these more massive stars will make it harder to detect exoplanets around using the transit method. The sensitivity of the telescope will determine the minimum sized planet we can detect around a star of a given temperature. The unique conditions of each observation will affect the noise present in the data, so a separate minimum detectable mass must be determined for each target (see Section 5.6). If we are able to estimate a star's luminosity based on its brightness and distance, we can also estimate its radius in solar radii using $R_* = R_\odot (T_\odot/T_*)^2 (L_*/L_\odot)^{1/2}$. These relationships will prove useful in ruling out planet detections based on radius. The time spent observing targets will factor into ruling out planets by period (see Section 5.7).

1.3.1 Spectra

The spectra of hot stars are shaped by the blackbody-like radiation curve associated with the temperature of the star and the atmospheric composition. The enhanced temperature of early-type stars shifts the blackbody curve of the stars to a higher energy region of the electromagnetic spectrum. O stars peak in the ultraviolet with A and F stars peaking closer to the blue part of the visible light spectrum. The higher energy radiation field will also affect the state of atoms

in the stellar atmosphere.

Cooler stars are dominated by absorption features due to bound-bound electron transitions. When a star absorbs a specific amount of energy, a photon is removed. When the electron de-excites to a lower energy level, it can reemit a photon. In early stars, however, the radiation from the star is so intense and at such high energy that elements are ionized, leaving only the hydrogen lines as prominent bound-bound opacity. Type A stars have the deepest hydrogen lines while O and B stars ionize too much hydrogen for bound-bound transitions to be as dominant.

In hot stars, opacities from the stellar atmosphere are continuous because they originate from ionization and free-electrons. Transitions between a bound and ionized electron state produce a saw-tooth pattern while transitions between the ionized states can scatter light proportional to ν^{-3} because the Planck function has this frequency dependence and we assume the material to be optically thick. This relationship means longer wavelengths of light are scattered more. For completely ionized electrons, light is scattered uniformly across all wavelengths. All these dominant forms of opacities in early-type stars yield more continuous spectra.

1.3.2 Variability of F-Type Stars

In the search for exoplanets, stellar temperatures of host stars are predominantly cooler because of the biases in our detection methods. Hot stars have a more continuous spectrum which makes radial velocity measurements more difficult. Additionally, hotter stars are more massive and have larger radii, making the transits of orbiting planets harder to detect. F stars can be considered hot in the context of the search for exoplanets and we begin this search with stars in

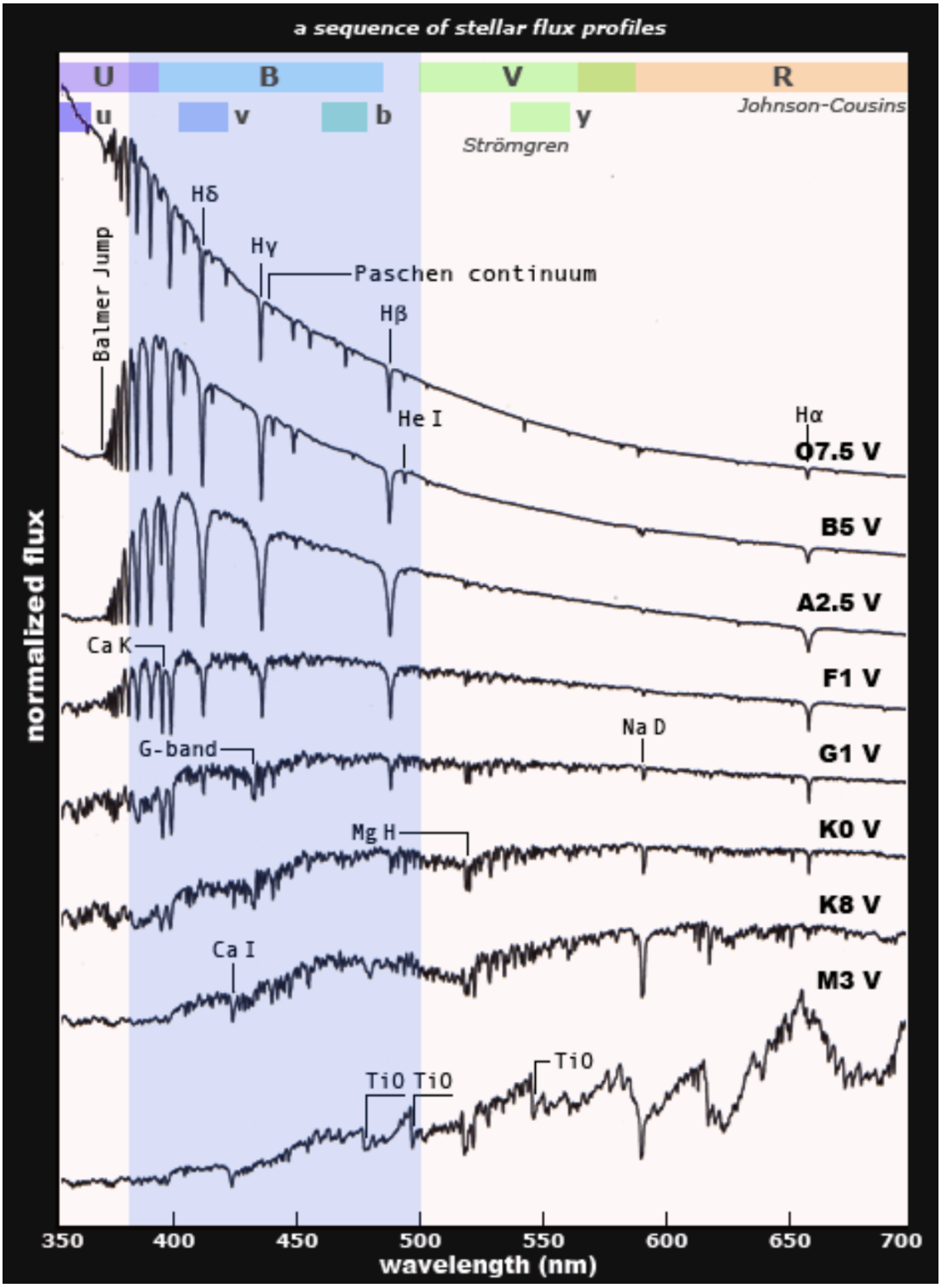

Figure 1.4: Hotter stars have more continuous spectra with higher energy wavelength peaks. This figure was produced by the Black Oak Observatory.

this spectral type. Understanding the variability common in F stars is important to discovering new variable stars while searching for exoplanets. The variability will also need to be subtracted from data of a planetary transit if an exoplanet detection is made.

The opacity bump, also known as the κ mechanism, is a common driver of pulsations in variable stars. An opacity bump happens when a layer of a star absorbs light, causing the layer to heat up and expand. As the absorbent layer expands, its opacity decreases, allowing heat to flow to outer layers and increase luminosity. Then it reaches a critical point where the pressure of the layer below the expanded layer decreases and the layer contracts. This process is called the Eddington Valve because the expanding layer acts like a valve that accumulates and releases heat periodically (Lee & Osaki 1982).

The layers required for this absorption are called envelopes. They are made of partially ionized gas. This partial ionization allows for some particles to ionize in the absorption phase, causing expansion due to heating. Then when elements return to their ionized state, opacity decreases and radiation flows out of the star while the layer begins to contract (Lee & Osaki 1982).

For cooler variable stars that utilize the Eddington Valve, called Cepheid variables, the envelopes that allow for opacity bumps are dominated by the HeII $\rightarrow$ HeIII ionization region (LeBlanc 2010). These variable stars are categorized as δ Cepheid variable stars after a star in the δ Cephei quadruple star system where this type of variability was first discovered. δ Cepheid variables are giant or supergiants and range in spectral class from F6–K2 (Rodgers 1957). The radius in which the envelope exists depends on the temperature of the star. Partially ionized envelopes too close to the core and envelopes close to the surface in the convective zone will not produce an opacity bump. For stars cooler than type-F,

the region where helium is partially ionized is near the core where the intensity of radiation is high. At these depths, the opacities have negligible effects on the luminosity at the surface of the stars because opacity-bump-driven fluctuations do not penetrate the thick layer of material between the partially ionized envelope and the photosphere. Stars hotter than late F stars will contain the envelope of partially ionized helium in the convective zone of the star, meaning there will not be the radiative absorption and emission needed to produce an opacity bump. F stars and giant G stars are the most common variable stars that use the opacity bump mechanism.

We see in Figure 1.5 the κ mechanism in action for the star δ Cephei. At the minimum radius, HeIII is dominant in the contracted shell. Since HeIII is more opaque than HeII, luminosity is near its minimum. As the opaque HeIII envelope absorbs radiation and expands, the radius reaches a near maximum and electrons recombine to form HeII. The HeII-dominated envelope is less opaque, causing luminosity to reach a near maximum. Then the envelope contracts and the process starts over again.

δ Cepheid variables have a period of variability from 1–100 days (LeBlanc 2010). The period of variability is a function of the radius and mass of the star as pulsations through a larger radius and more massive stars will take longer to propagate. Since radius and mass are related to luminosity, δ Cepheid variables could be used as standard candles by deriving the period-of-variability-luminosity relationship from parallax measurements of nearby δ Cepheids. This variability-luminosity relationship is named the Leavitt law after its discoverer Henrietta Swan Leavitt.

δ Cepheid variables are large stars, making detections of planets around these stars difficult. However, there exist variable stars still on the main sequence that

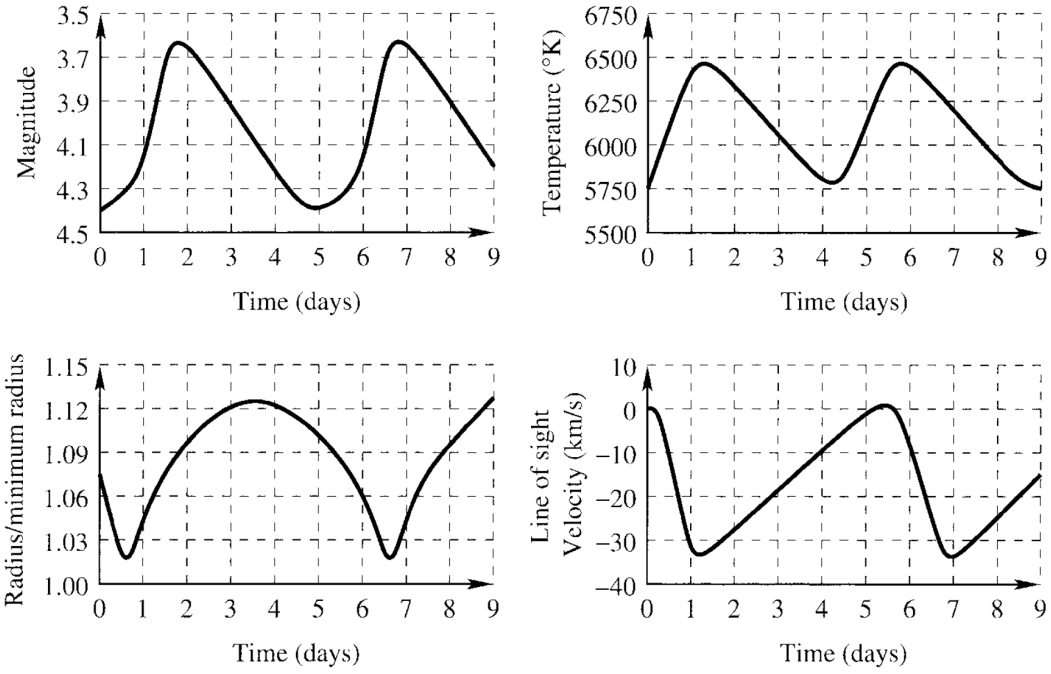

Figure 1.5: Plot from LeBlanc (2010). Shows the variation in brightness, temperature, radius and velocity over the period of variability for the classical Cepheid star δ Cephei.

use the same κ mechanism with partially ionized helium envelopes to produce variability. They are made up of main-sequence or near main-sequence A and F stars with a period of pulsations from 0.02–0.3 days (Catelan & Smith 2015). These pulsations have V_{mag} amplitudes from 0.003–0.9 (Poro et al. 2021). Since this survey focuses on main sequence stars, these periods and variations in magnitudes are more likely to show up in the data than the variability found in δ Cepheid stars.

A newer and less understood classification of variable F-type stars is γ Dor stars named after the star γ Doradus. These are F0 to F2-type main-sequence or near main-sequence stars with periods of 0.4–3 days (Catelan & Smith 2015). These variations peak around 0.1 magnitude and are suspected to be produced by non-radial gravity waves called g-mode oscillations or some other unknown mechanism (Krisciunas 1993). Non-radial oscillations mean they do not travel in spherically symmetrical pulsations but are instead refracted due to the pressure gradient in stars that alter the speed of sound through the star (Catelan & Smith 2015). Gravity waves arise from the buoyancy of material in the star driving the movement of material.

While there are several examples of variable F-type stars on and off the main-sequence, they are rare occurrences and for the most part, main-sequence F-type stars are not highly intrinsically variable. Additionally, the magnetic fields of F-type stars are weaker, meaning starspots that can cause rotational variability are less prevalent (Seach et al. 2020). Observations of F-type stars by Giampapa & Rosner (1984) could not detect starspots implying they were small and evenly distributed or not present. This means photometric observations of most F-type stars are likely to require minimal variability corrections for long-term transit observations.

1.4 Overview

With Wesleyan University's 24-inch research telescope, we have the opportunity to invest time into surveying early, bright stars to search for planets at the limits of our detection techniques. By observing individual targets, bright stars can be properly exposed for without reaching the saturation limit. As the telescope is configured to be more automated, observations can occur at any point in the night based on weather condition monitoring. With enough observations, transiting exoplanets of a given size and period can be ruled out.

In Chapter 2, I will go over how I built the sample of bright early-type stars and how I chose suitable targets. In Chapter 3, I discuss the telescope, its properties and the type of data I will be taking. In Chapter 4, I discuss the program I used to reduce the data and programs I have developed to test the sensitivity and probability of detection. In Chapter 5, I go over the observations that have been processed thus far and use the programs discussed in Chapter 4 to analyze the data. In Chapter 6, I conclude with a discussion of why a detection would be significant and future work.

Chapter 2

Building the Sample

The temperature-magnitude space where the radial velocity and transit methods have their deficiencies encompasses many stars. In this chapter, I shall examine which stars should be given priority in this search and go over the process I use to determine suitable targets.

2.1 Stellar Parameters

2.1.1 Temperature

Utilizing effective temperature as criteria for my stellar sample requires balancing making detections in temperature regions where detections are rare while still observing stars with radii small enough to produce detectable exoplanets. Looking at temperature in the context of exoplanet discoveries, it becomes clear that stellar temperatures above 6,500 K (type F5V) are rare in terms of radial velocity detections with only two detections and one detection above 6,560 K (type F4V based on data from Pecaut & Mamajek (2013)). Meanwhile, the transit technique has 643 detections of planets at stellar temperatures above 6,500 K and 447 detections for stars above 6,560 K. As temperatures increase, the stellar radius increases as well. This relationship can be estimated using the luminosity equation for a black body:

$$R_* = \sqrt{\frac{L}{4\pi\sigma T^4}}. \tag{2.1}$$

For now, we can use this simple relationship to think about how radius grows with temperature and temperature but in Section 3.4, I derived the empirical equation for R_* that is just a function of temperature. To remove the dependence on luminosity from this equation, I used empirically measured relationships for mass and luminosity along with mass-radius relationships to derive Equation 3.6, which is $R_*(T)$. I can convert this stellar radius to an estimated minimum detectable radius by assuming a certain transit depth threshold for which detections of smaller transit depths cannot be identified.

The planetary alignment is dependent on the radius of the star and the semi-major axis. The probability that a planet will be transiting is simply R_*/a where R_* is the radius of the star and a is the semi-major axis (Stevens & Gaudi 2013). If we calculate the semi-major axis at some fixed period P and stellar mass as a function of temperature $M_*(T)$ using

$$a = \left(\frac{GM_*(T)P^2}{4\pi^2}\right)^{1/3} \tag{2.2}$$

and using the equation for stellar radius as a function of temperature, we can derive a probability of a planet being transiting as a function of stellar temperature.

Using a minimum detectable transit depth of 0.33% which was estimated from a portion of the preliminary data using methods described in Section 4.4, I plot in Figure 2.1 the estimated minimum detectable radius as a function of temperatures. On the same graph, I plot the probability that a planet orbiting with a 1 day period around a star of mass $M_*(T)$ is a transiting planet.

From Figure 2.1 we see the minimum radius required to make a detection

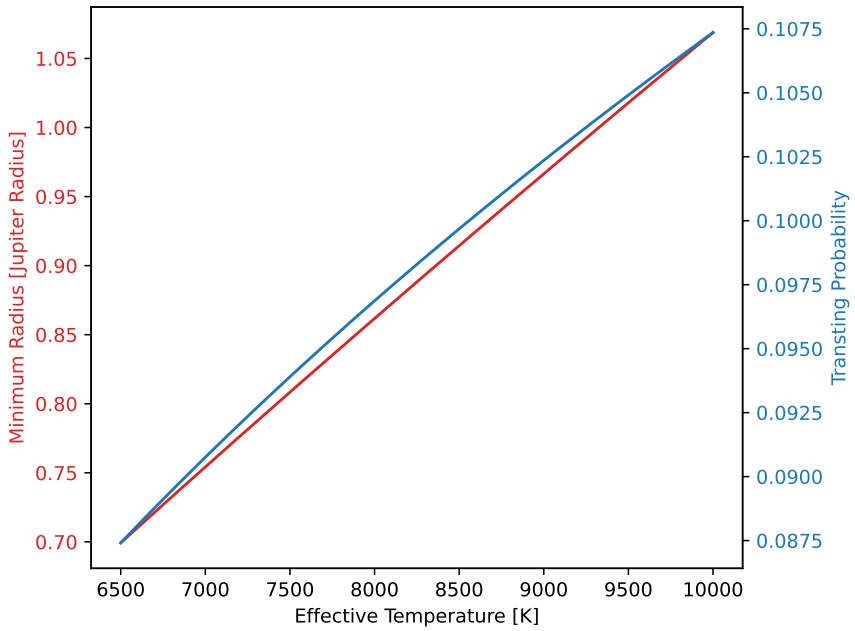

Figure 2.1: (red) Minimum detectable radius and (blue) probability a 1 day period orbiting some star with mass $M_*(T)$ is transiting both as a function of temperature.

increases by about 30% while the probability of the planetary system being aligned goes up by about 20% for temperatures between 6,500 and 10,000 K. For the targets chosen in this initial search, I chose to favor stars closer to 6,500 K in favor of minimizing the size of the planet that can be detected over the probability the planetary system will be properly aligned. Looking at many targets will increase the likelihood that we find a transiting system.

2.1.2 Brightness

The radial velocity technique has no trouble making detections around bright stars. In fact, the enhanced brightness increases the signal-to-noise of the spectra, making detections more significant. Figure 2.2 shows radial velocity detections peak around a V Magnitude of 8 and many discoveries made around stars brighter than this peak.

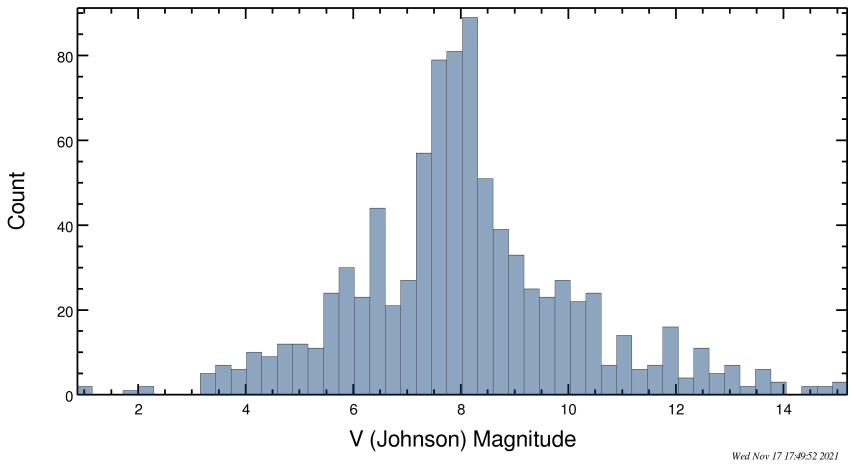

Figure 2.2: Histogram generated by the NASA Exoplanet Archive of exoplanet discoveries via radial velocity method by host star V magnitude

Meanwhile, the most successful transit searches have been designed for dimmer stars, peaking at a $V_{\rm mag}$ of around 15 as shown in Figure 2.3. For stars brighter than 15th magnitude, discoveries fall off quickly, nearly dropping to near zero for stars brighter than $V_{\rm mag} = 8$. Only 30 planets have been discovered around these bright, $V_{\rm mag} < 8$ stars via the transit method.

To account for the two biases in temperature and magnitude, we constrained the sample to $T_{\rm eff} > 6,500$ and $V_{\rm mag} < 8$. The final result is a sample of stars not yet known to host exoplanets that occupies a district region of stellar temperature-magnitude space for detected exoplanets. In Section 2.4, I plot again Figure 1.3 with the stars in this sample that are suitable to observe for at least five hours on the night of 2021 Nov 12 at Van Vleck Observatory. We see that the stars in the sample of bright, early-type stars are in a distinct region of this plot where there is a complete lack of exoplanet discoveries. Making an exoplanet detection around one of these stars would be significant.

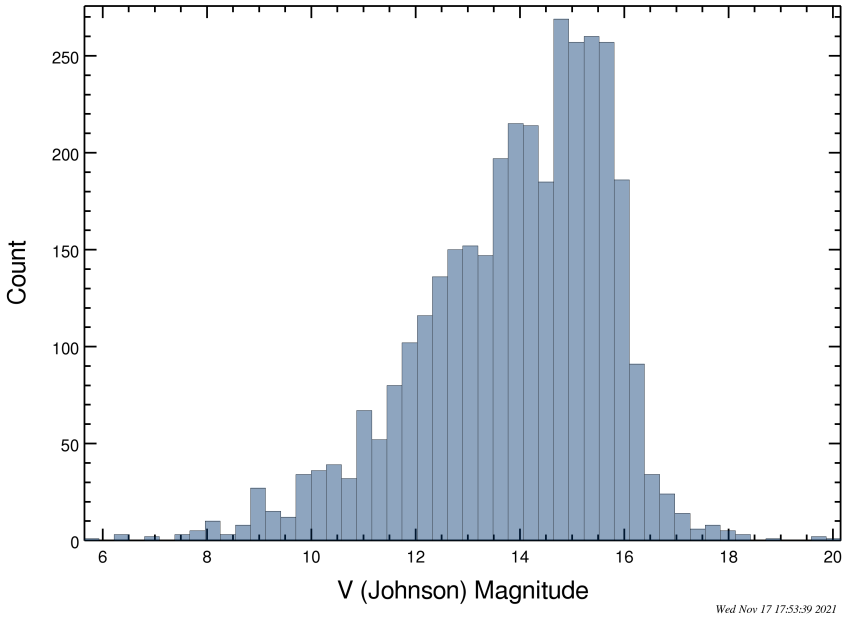

Figure 2.3: Histogram generated by the NASA Exoplanet Archive of exoplanet discoveries via transit method by host star V magnitude

2.1.3 Stellar Rotational Velocity

$v \sin i$ is a measure of the stellar rotational speed times the sine of inclination. Inclination is the angle from the pole of the star to the line of sight of the observer. When a star has an inclination of 0°, the observer is looking right at the pole of a star. When the inclination is 90°, the equator of the star is facing the observer.

The reason we measure rotational speed with $\sin i$ is because rotation is typically measured by observing the rotational broadening of a spectral line which is a form of Doppler broadening. Doppler broadening is caused by motion that is radial to the observer so we need to add a $\sin i$ coefficient to specify that we are only measuring rotation that is radial to us. If there is no rotational broadening, it is unlikely the star is not rotating, particularly for early-type stars which have

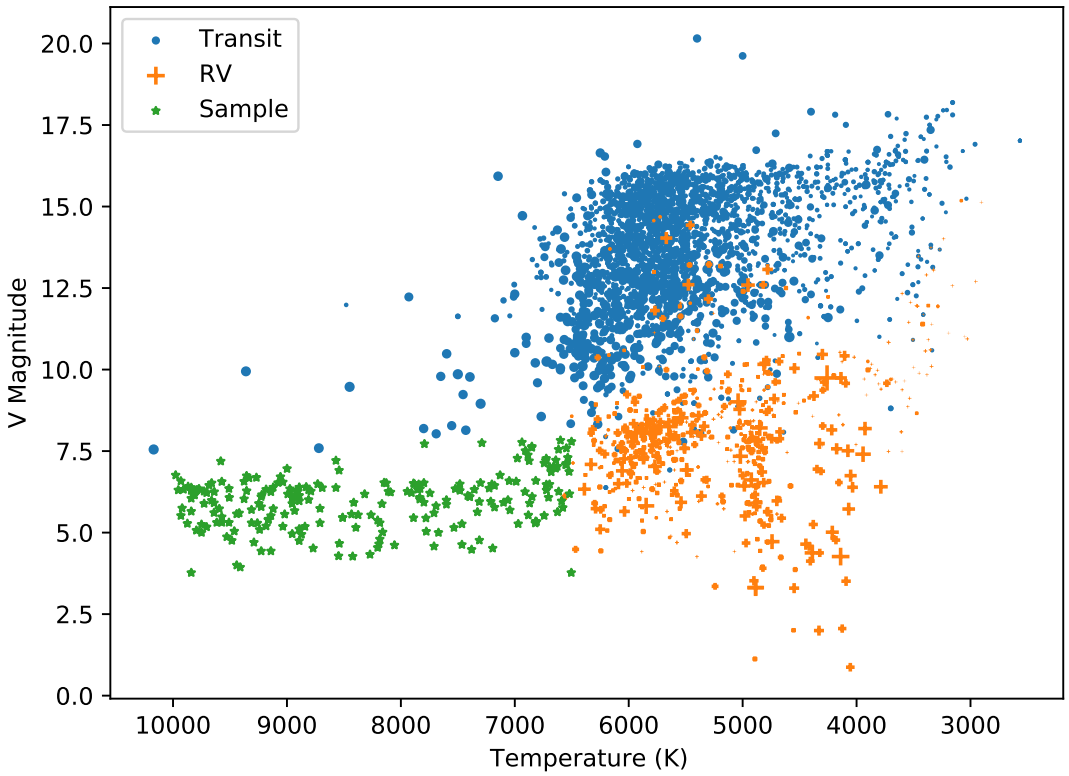

Figure 2.4: Figure 1.3 plotted with stars in the early bright sample (in green) suitable to observe for at least five hours the night of 2021 Nov 12 at Van Vleck Observatory. The size of the blue dots is proportional to the transiting planet's radius while the size of the orange crosses is proportional to the mass of the planet times the sine of the planet's inclination.

high rotational speeds.

Plotted in Figure 2.5 are all the stars in the early bright sample. I estimated the envelope that encloses these stars where $v \sin i$ is maximized at each effective temperature, representing the approximate rotational velocity as a function of temperature. Along this envelope, it is more likely that the star has an inclination of 90° because if each star at a given temperature has a similar rotational speed, the $v \sin i$ will be maximized when $i = 90°$.

This relationship between stellar temperature and rotational speed is described by McNally (1965) and the angular momentum of different spectral types is observed. As outlined by Weber & Davis (1967), stars lose angular momentum as they age through interaction with surrounding material and material ejected from the star. Hot stars have existed for less time, meaning they exhibit faster rotations.

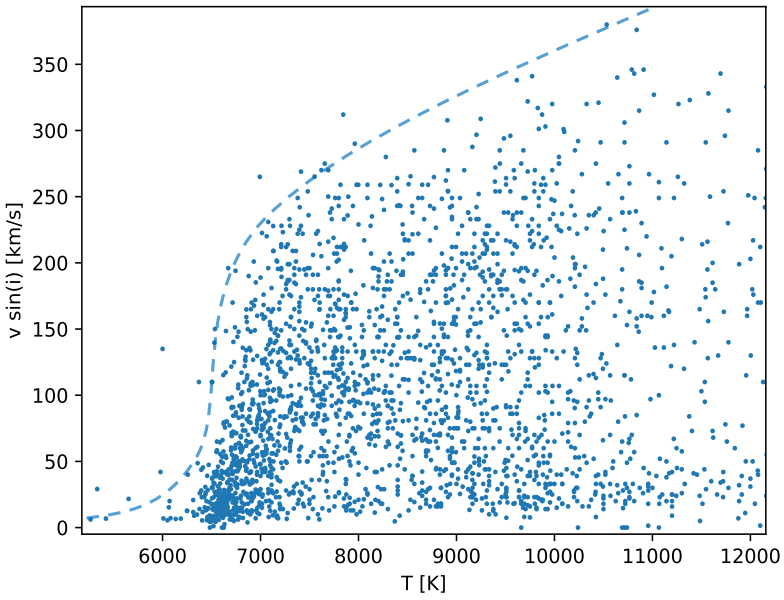

Figure 2.5: $v \sin i$ versus temperature plotted for star within the early bright sample. The approximated envelope that encloses the stars is plotted as a blue dotted line.

2.2 Target Acquisition Program

I designed a `Python` program that outputs a list of targets suitable to observe on any given night along with key observational and stellar properties. Stars that met the $T_{\rm eff}$ >6,500 and $V_{\rm mag} < 8$ criteria were downloaded as a VOTable from SIMBAD with key parameters like their equatorial coordinates, $T_{\rm eff}$ and $v \sin i$. These stars were then loaded into a `Python` script using the `Astropy` package. The time of sunset was obtained for a given day using the `suntime` `Python` library and the local sidereal time was calculated. Parsing through the VOTable, stars off the main sequence were removed. Airmass was calculated over the course of a night and stars that were below the horizon or never had an airmass below 1.5 for more than five hours were removed from the sample.

Stars that met these initial criteria for a given night of observation were then examined to see if there were sufficient reference stars for photometric observations. Using the `astroquery.gaia` `Python` library, we searched a 24' (the telescope's field of view) box around the target star and counted the number of stars below a $G_{\rm mag}$ of 15, 12 and 9. Stars that had no reference star or only one reference star between a $G_{\rm mag}$ 15 and 12, were removed.

Finally, all the stars were printed along with their coordinates, the time the target rises, the number of hours over the course of the night where airmass was below 1.5, $V_{\rm mag}$, $T_{\rm eff}$, $v \sin i$ and the number of reference stars. Using these constraints, there are enough listed properties to make an informed selection of a target suitable for observation on any given night. For example, on 2022 Apr 13, there were 244 potential observing targets with temperatures between 6,500 and 10,000 K. The median temperature of these stars is 7,893.5 K and median $V_{\rm mag}$ of 6.054. There is a median of 3 reference stars with $G_{\rm mag} < 15$ for each target on

this night.

Chapter 3

Telescope Properties

Small automated telescopes can play an important role in conducting low-cost surveys and follow-up observations with great flexibility. Small telescopes are sensitive enough to acquire scientific data on astronomical phenomena that can motivate follow-up studies with more sensitive equipment. The MEarth project conducted by Nutzman & Charbonneau (2008) used two observatories in the northern and southern hemispheres each with eight 16-inch telescopes, leading to the discovery of several exoplanets around M dwarf stars and analysis of the M dwarf target stars themselves. Villanueva et al. (2016) use an automated 20-inch PlaneWave telescope for their DEdicatedMONitor of EXotransits and Transients (DEMONEXT) program to provide follow-up observations of transiting planets and transient events. The telescope is equipped with a spectrometer for studying the atmospheres of hot Jupiters and configured to confirm "supernovae, flare stars [and] tidal disruption events" identified by the All Sky Automated Survey for SuperNovae (Kochanek et al. 2017). With the success of past automated small telescope observation campaigns, this transit survey of early bright stars has the potential to make significant discoveries. In this chapter, I will explain the properties of the telescope, issues that have arisen, the automation of the telescope and detection limits.

3.1 Specifications and Controls

Wesleyan University's latest 24-inch telescope was installed in 2020. It was manufactured by PlaneWave instruments as part of the CDK600 Observatory system. The mirrors are made of fused silica to reduce thermal expansion. The CDK24 optical tube features an $f/6.5$ aperture and 3974 mm focal length. The f-number $f/6.5$ is the telescope's aperture diameter divided by the focus length. Focal length is a measure of how strongly a telescope focuses light on the sensor. The inverse corresponds to the telescope's optical power (Greivenkamp 2004). The 24-inch PlaneWave telescope has about half the focal length of Wesleyan's previously operated Perkin 24-inch telescope, giving the new telescope twice the optical power, allowing the telescope to gather more light in a shorter amount of time.

The L-600 telescope altitude-azimuth (alt-az) mount is driven magnetically, allowing it to operate without gears. Without the motors engaged, the telescope can glide freely and can be manually moved. When engaged, the telescope can point precisely with sidereal tracking. The telescope can slew up to a speed of 50 degrees a second. The telescope has four optical ports for instrument mounting. Currently, two of the ports are occupied by the CCD and eyepiece. The field of view of images taken with the CCD is 23.9 by 23.9 arcminutes. The instrument side of the telescope rotates to allow for proper configuration of the viewing eyepiece and continuous sidereal tracking for this alt-az mounted telescope.

The telescope is controlled through two pieces of software: PlaneWave Instruments 3 (PWI3) and PWI4. PWI3 controls the focuser and rotator and PWI4 controls the telescope pointing. A separate program controls the optical port switcher which moves a mirror to direct the collected light to one of the four

ports. The dome can rotate freely in both directions. The shutters receive power at any azimuth angle through a charged track, allowing them to open and close in any position. The dome is controlled through the Maestro program which operates the azimuth angle and the upper and lower shutter.

3.2 Photometry

Photometry is a method for measuring the apparent flux of an object and is the key piece of data collected for this survey. Photometry relies on taking images of a field of stars and comparing the relative flux received from each source. Stars that are used to compare flux to the main target are called reference stars. Conditions that affect the entire image taken with a CCD are removed from photometric measurements using reference stars. For example, atmospheric scattering and absorption that uniformly darkens the image will not change the relative brightness of the main target compared to the reference stars because all objects in the field of view are affected in the same way. So as an object changes airmass over the course of a night, the photometry will be minimally affected by the atmosphere.

A simple method for calculating the relative flux is to use the ratio of total counts from each pixel of the target star to the total counts of the reference stars:

$$F_{\text{rel}} = \frac{F_{\text{target}}}{\sum F_{\text{ref}}}. \tag{3.1}$$

The more reference stars, the less one star's variation will affect the relative flux of the target. Since these units of flux are often arbitrary as properties like atmospheric, CCD thermal variations and changes in reference stars used between observations will change these flux values, it is common to normalize relative flux when processing data.

Photometry is often conducted using the Johnson-Morgan bands. These are filters that let in a broad selection of wavelengths. They are enumerated by letters: U for ultraviolet, B for blue, G for green, V for visual, R for red and I for infrared. Their response pattern across relevant wavelengths is displayed in Figure 3.1. The blackbody curves relative to a B-type star are displayed in the same figure. Despite the larger wavelength bands being further from the peak wavelength flux for early-type stars, hot stars radiate at higher luminosities at all wavelengths.

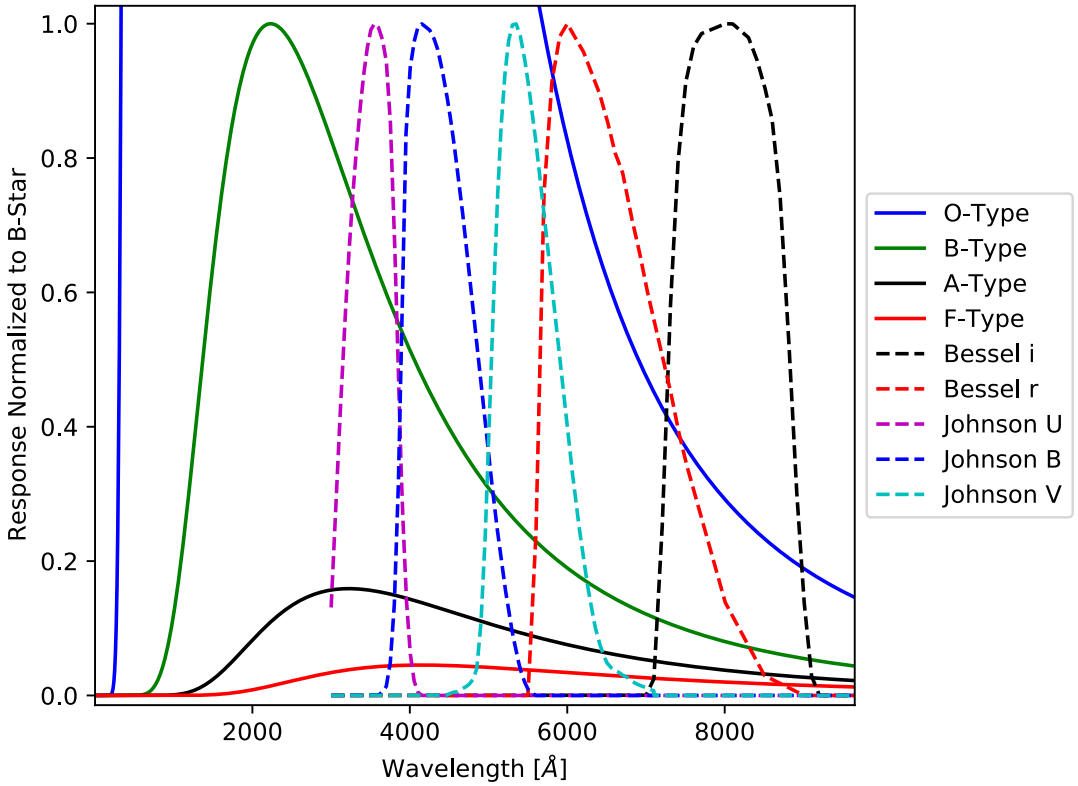

Figure 3.1: Johnson-Morgan filter response patterns plotted with blackbody curves for different spectral types. Response patterns are normalized to each of their peaks and blackbody curves are normalized relative to the peak of the B-type star curve.

For conducting photometry of early stars, using a U or B filter will capture more signal as hotter stars peak at these higher energies relative to cooler stars. However, photometry relies on reference stars which are usually cooler because

late-type stars are far more abundant. Hot stars are more luminous as well, so depending on the distance of the star, it may still produce a high signal-to-noise ratio to use a longer wavelength spectral band to boost the signal from less luminous, late-type stars. The issue with shorter wavelength spectral bands is light at higher energies becomes scattered by a factor of λ^{-4} in a process called Rayleigh scattering (Young 1981). The V-filter is commonly used for photometric measurements because it is in the middle of the visible spectrum and strikes a good balance for exposure of many spectral types at once. For this survey, observations will be taken in the V band.

3.3 Telescope Errors

Early observations with the PlaneWave telescope revealed several issues with the telescope, dome and weather station. Observations were first made directly in the imaging software MaxIm DL to control the CCD and relied solely on the PlaneWave software for tracking and focusing. In the fall of 2021, the program Astronomy Control Panel was implemented to control PlaneWave and Maestro software while adding functionality like plate solving for pointing corrections and automated weather-dependent observing.

3.3.1 Rotation

De-rotating the CCD to compensate for the change in orientation of the field ensures the starlight falls on the same group of pixels throughout the night. When taking long time-series observations using PWI4 for tracking, the telescope would stop rotating towards the end of observation, causing rotation about the center of the image.

The rotator mechanism was tested to see if there was an issue with the motor, causing the rotator to de-rotate at an insufficient rate. No mechanical issues were found. A potential error was in PWI3 reading of the position of the rotator. Homing the rotator allows PWI3 to recalibrate the rotator's position angle but the issue persisted.

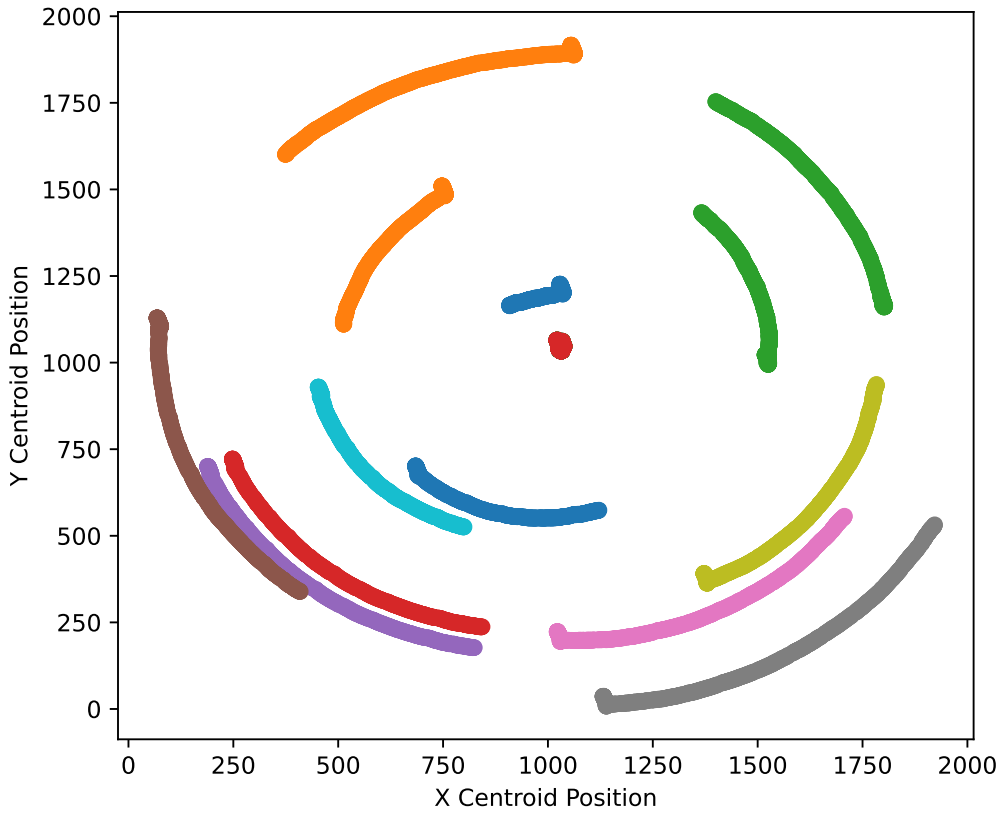

Figure 3.2: A scatter plot of the positions of the target star (in the center) and every reference star in each image of an observation of a WASP-65 b transit on 2021 Mar 13. This night shows the issue with the telescope not de-rotating the image to maintain the positions of stars on the CCD throughout an observation.

After investigating further, we discovered the de-rotation issue was caused by choosing an initial position angle that led the rotator to reach the limits of its

rotation range. Position angle is used to measure the angle of the rotator. It is the difference in the right ascension with the image and the north celestial pole measured in positive RA with the top of the image representing the direction of positive declination. The way the telescope is configured, a position of 90 degrees can be maintained throughout a night of observing, allowing ample rotator range to de-rotate. To assist in ensuring the position angle is maintained at a reasonable value, PWI3 is configured to maintain this position angle when slewing between targets. For stars below the north celestial pole, the position angle is offset by 180 degrees to prevent the sensor from flipping. For these northern stars, the optimal position angle becomes 270 degrees.

3.3.2 Telescope Automation

Astronomy Control Panel (ACP) is a powerful piece of software that combines the functionality of dome and telescope control with scripting and automation. When ACP is running, it connects to the telescope and rotator through PlaneWave software, the CCD through MaxIm DL, the dome through Maestro, and weather data by reading a single-line weather status file. Because of issues with the ClarityII weather hardware installed with the telescope, the weather station is not connected during setup to prevent inaccurate weather data from interfering with observations.

To run observations on ACP, several pre-programmed JavaScript files are called to direct the desired operations. `AquireImages.js` is the most commonly used and versatile script. When run within ACP, you are asked to select a file that contains a list of commands that calls functions within the `AquireImages.js` script. These commands, called directives, can tell ACP to open and close the

dome, cool the camera and take science or calibration images.

Built into ACP is a flat acquisition protocol that when running, points the telescope near the zenith opposite to the direction of sunset/sunrise and takes sub-array images to gauge the median counts of the image. When the median pixel value is at 35,000 counts per pixel, full-frame flats are taken in the specified bands. This script automates one of the most involved procedures in observation. No longer does an observer need to continually monitor the counts of flat frame images to decide when to start collecting them. ACP can automate the process in every band of observation. To ensure that the proper sky illumination level is captured for each band, the flat acquisition program takes flats in order of the least to most sensitive bands for dusk flats and in reverse order for dawn flats.

The shutdown of the telescope is also well integrated into ACP. By adding the `#shutdown` directive into an observing plan, ACP will park the telescope and dome, close the dome and warm up the sensor. However, ACP is not fully configured to startup and completely power down the telescope and dome. After the `#shutdown` directive is fulfilled, we must close all Maestro and PlaneWave software and turn off the power that connects to the telescope and dome. For startup, the power must be turned back on and the software must be reopened and connected to ACP.

Once the final pieces to the startup and shutdown procedure are automated into ACP by editing the code, full automation can be achieved through the use of ACP Scheduler. The Scheduler can take multiple targets and observational constraints and choose for itself which targets to observe given the orientation of the objects and rankings specified by the user. Using the Scheduler, the telescope will be able to open up by itself when the weather clears to take observations at any moment. The issues with the weather station have delayed the implementation

of the Scheduler and ACP requires current and safe weather for the Scheduler to dispatch jobs. To trick ACP into running, I created a fake weather station that takes local weather data and writes a weather file in the same format as CarityII but with the rain and cloud flags updated to local weather. The local weather is only updated every 10 minutes so this workaround cannot be used without supervision.

Full automation will dramatically increase the amount of data that can be acquired on a nightly basis. The pilot observations I will present in Chapter 5 were obtained with ACP scripts with human supervision. Most observations only lasted 5 hours despite clear sky conditions because it was infeasible to stay awake entire nights consecutively. With a trusted weather station, the telescope will be able to observe entire nights, switching between targets that maintain a suitable airmass. All the infrastructure to create automated observing programs is working in ACP. Once we have a working weather station, the automation can be quickly implemented.

3.4 Detection Limitations

The limits on detections are a function of several factors. Variations in the data collections will be produced by the atmospheric conditions of any given night and the errors produced by the CCD. Intrinsic properties of the stars will add variation and determine the potential depth of a transit. Variable stars with short period variabilities will need to be categorized so possible transits can be detected. By measuring the sources of error in the data and accounting for stellar variability, a minimum planetary radius can be determined.

Each star in my sample has a temperature measurement. To determine the

size limit of a detectable planet, we need to derive the transit depth given by Equation 1.2. Knowing the radius of the planet and the standard deviation of photometry measurements, we can derive the minimum planetary radius by re-arranging Equation 1.2:

$$R_p = R_* \sqrt{\delta}. \tag{3.2}$$

To get this equation in terms of stellar temperature, I derived stellar radius as a function of temperature relation by combining Stefan–Boltzmann's law ($L = 4\pi R^2 \sigma T^4$) with mass-luminosity and mass-radius relationships for stars from Demircan & Kahraman (1991):

$$L/L_\odot = 1.02(M/M_\odot)^{3.92}, \tag{3.3}$$

$$R/R_\odot = 1.33(M/M_\odot)^{0.555}. \tag{3.4}$$

The result is a nearly linear function for stellar radius in terms of temperature in Kelvin:

$$R/R_\odot = 2.44(\sigma R_\odot^2/L_\odot)^{0.198} T^{0.790}. \tag{3.5}$$

Using this equation, there is a deviation from the range of stellar radius values published in Habets & Heintze (1981). To correct for this, I plugged in the estimated minimum temperature for F-type stars of 6,000 K from Habets & Heintze (1981) to Equation 3.5 to derive an offset factor of $0.379 R_\odot$. The altered equation aligns more closely with ranges derived from eclipsing binaries. With this offset, the Equation 3.5 becomes:

$$R/R_{\odot} = 2.44(\sigma R_{\odot}^2/L_{\odot})^{0.198} T^{0.790} + 0.379. \tag{3.6}$$

The photometric sensitivity can be obtained by first injecting transits of varying depths using the transit curve modeling `Python` package `batman` created by Kreidberg (2015). Then identifying the minimum planet-to-star radius ratio that can be detected using the box leased squared method in the `Astropy Python` package. This photometric limit is combined with the estimated stellar radius derived from Equation 3.6 to find a planetary radius. The details of this process are discussed in Chapter 4 along with all the other programs utilized for data processing. As described in Section 2.1.1, Figure 2.1 was generated using Equation 3.6 and preliminary results from injecting transits. In the next chapter, I will describe the injection process in detail and in Chapter 5, I will go over a more detailed calculation of the telescope's sensitivity using all the processed data available.

Chapter 4

Analysis

The data analysis pipeline requires data reduction, modeling and simulation. Raw observations are first corrected using calibration images and then the flux of the target star is measured using differential photometry. These data reduction steps are done using the program `AstroImageJ` developed by Collins et al. (2017). The second stage of analysis utilizes several programs that I have developed to search for potential transits in the data, find the minimum planet size that can be detected and simulate the probability that transiting planets would be detected. Using this approach, I will examine what type of planet discoveries are possible with my search, how to decouple stellar variability from planetary transits and how to identify or rule out transits.

4.1 Data Reduction

Each image must be calibrated to correct for the non-uniform illumination pattern and the noise produced from reading out the CCD and the temperature of the sensor. Flat field images are used to correct the raw data for the illumination pattern of the telescope. Light falls on the CCD sensor based on how it travels through the telescope, reflecting off mirrors and passing through filters. In addition, the performance of each pixel is not uniform (Chromey 2016). A flat field image is taken during dawn or twilight while the Sun is below the horizon but

the sky is still illuminated. An image is taken near the zenith where the scattered light from the Sun is nearly uniform so that the spatial variation in light received by the sensor is dominated by the artifacts of the telescope.

The exposure time for a flat field image is predetermined but the image must be below the saturation limit where there is a non-linear response to light. To find this precise moment where sky brightness is optimal, images are taken repeatedly after Sunset until the maximum counts per pixel are below 35,000, well below the saturation limit of 40,000 counts per pixel. Flats field images are taken using the expected exposure time and filter band that will be used during observations.

Bias frames are collected to subtract out the noise produced by reading out the sensor (Chromey 2016). Bias frames are acquired by setting the exposure time to zero so the signal in the image is dominated by the noise produced from reading out the sensor. Dark frames also correct for noise but are exposed for longer. Longer exposures capture the noise produced mainly due to the temperature of the sensor because the energy of electrons in the CCD increases with temperature (Chromey 2016). Reducing thermal noise is the motivation behind maintaining a cool CCD during observation. The CCD must be cooled to the temperature at which observations will occur so the calibration frames will capture the correct level of noise. Like flat field images, the exposure time for dark frames is set to the expected exposure time for observations.

To perform the corrections on the raw data, some math must be done on the raw calibration frames. The median value for each pixel is taken between each of the dark, bias, flat frames. Typically 15 dark and bias frames are acquired while 5 flat frames are taken due to the variable sky brightness as the Sun sets/rises. Finding the median across these images removes anomalies present in individual pixel values. Taking the medial pixel value is preferable to taking the average so

that outlier pixel values do not skew the median pixel value. Once these median calibration images are finalized, data reduction can proceed on the raw images as outlined in Chromey (2016).

First, the master bias is subtracted from the raw image as well as the median dark images because the noise from the readout will be present in both images. Then the de-biased median dark images are subtracted from the raw images. Now the non-uniform illumination pattern must be corrected. The median flat must first be normalized by dividing each pixel in the median flat by the median pixel value of the median flat. Then the science images are divided by the master flat so that the flux received on one part of the sensor has the same responses as any other point on the sensor. This way, deviations in the position of stars on the sensors due to tracking errors will not affect photometric measurements. This process is completed using the `AstroImageJ` Astronomy Data Processor plugin.[1]

4.2 Differential Photometry in `AstroImageJ`

With the processed data, I use `AstroImageJ` to conduct multi-aperture photometry. As described in Section 3.2, by comparing the flux of the target star to the flux of reference stars, we can extract a flux time series that reduces the effect of atmospheric conditions on the flux received. An example image of the target star HD 6314 and the reference stars used to process the data is displayed in Figure 4.1. After selecting an initial set of reference stars, `AstroImageJ` moves between images rapidly, re-centering the centroid positions across images. After the process is done, a file is produced with data on the relative flux along with a variety of other parameters like centroid positions of each target, the full width

[1] https://www.astro.louisville.edu/software/astroimagej/

at half the maximum (FWHM) and airmass.

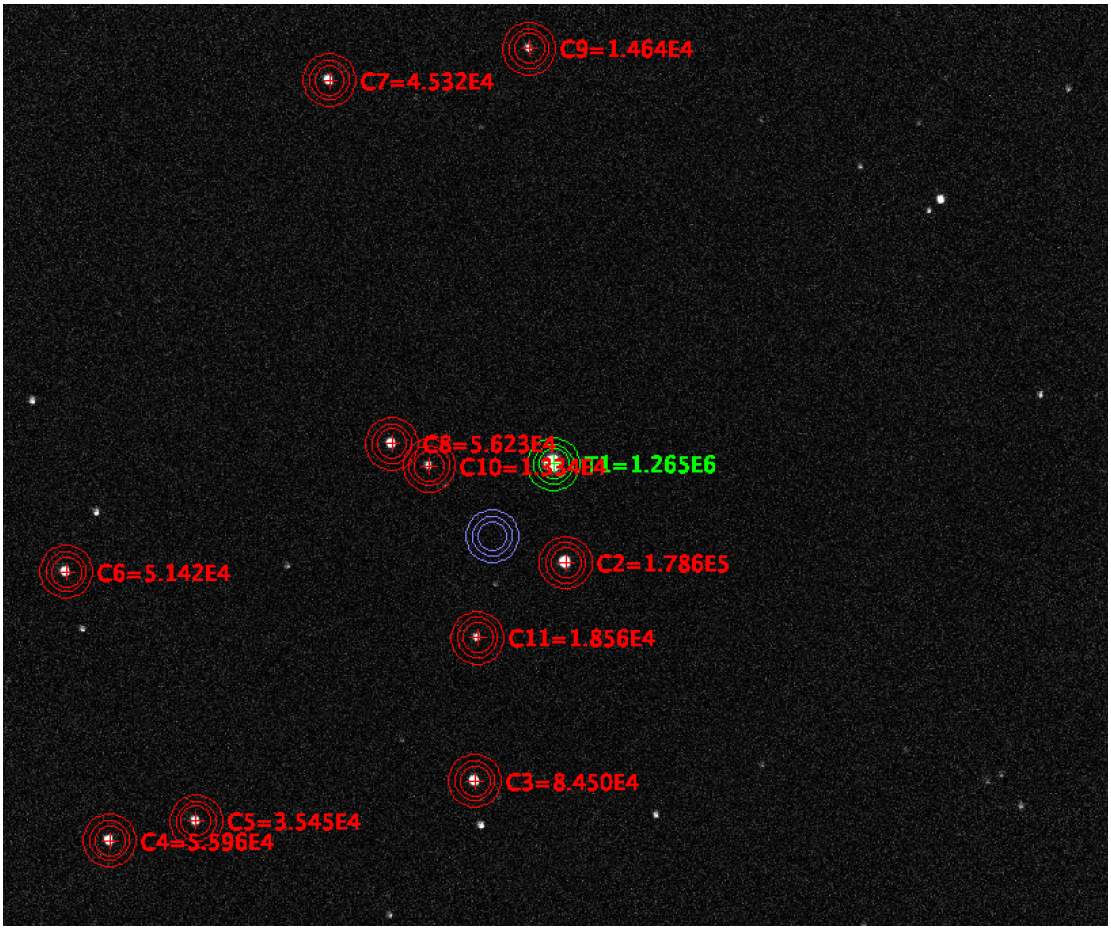

Figure 4.1: Image of the photometry apertures used to measure the relative flux of HD 6314 on 2021 Dec 12. The green aperture measures the brightness of HD 6314 while the red apertures measure the brightness of each reference star.

The error for each photometric measurement is calculated within `AstroImageJ` using the revised CCD equation from Merline & Howell (1995) which incorporates the CCD properties and the chosen aperture. Key properties of the telescope used in error calculations are the gain of 1.2 electrons per count and the readout noise of 7 electrons. The number of pixels used for each aperture factors into the random error. The counts from background pixels provide an estimate of the noise intrinsic to the sensor. Error is calculated for each aperture measurement

and then propagated through to the calculation of relative flux for the target star (Collins et al. 2017). After these differential photometry measurements are made, the data is ready to be analyzed through the programs I developed to look for transits and test the limits to what can be detected.

4.3 Analysis Scripts

In this section, I will describe the development and functionality of programs I have written to analyze the data I have collected. The findings derived from these programs will be discussed in the results in Chapter 5.

4.3.1 Diagnostics

The diagnostic program takes the photometric data and produces several plots as an initial check of the data and anomalies in the telescope tracking. The first two plots are the relative flux of the target over time. One is unbinned data so the full spread of data points is visible. The other time series plot is binned so the smaller scale fluctuations can be more easily visible. Figures 4.2 and 4.3 display these first two plots for the target HD 206751 for observations on the night of 2021 Oct 6. The light curve for Figures 4.2 and 4.3 show that this night of observation had particularly flat light curves, making HD 206751 a great target for transit detections.

The next figure produced by this program is a graph comparing the error calculated by `AstroImageJ` to the standard deviation of the data across varying bin sizes. A similar method of error analysis is done by Fukui et al. (2016) to identify sources of noise. In Figure 4.4, we see that for the same observation of HD 206751, the standard deviation and the error diverge past a bin size of 5. This

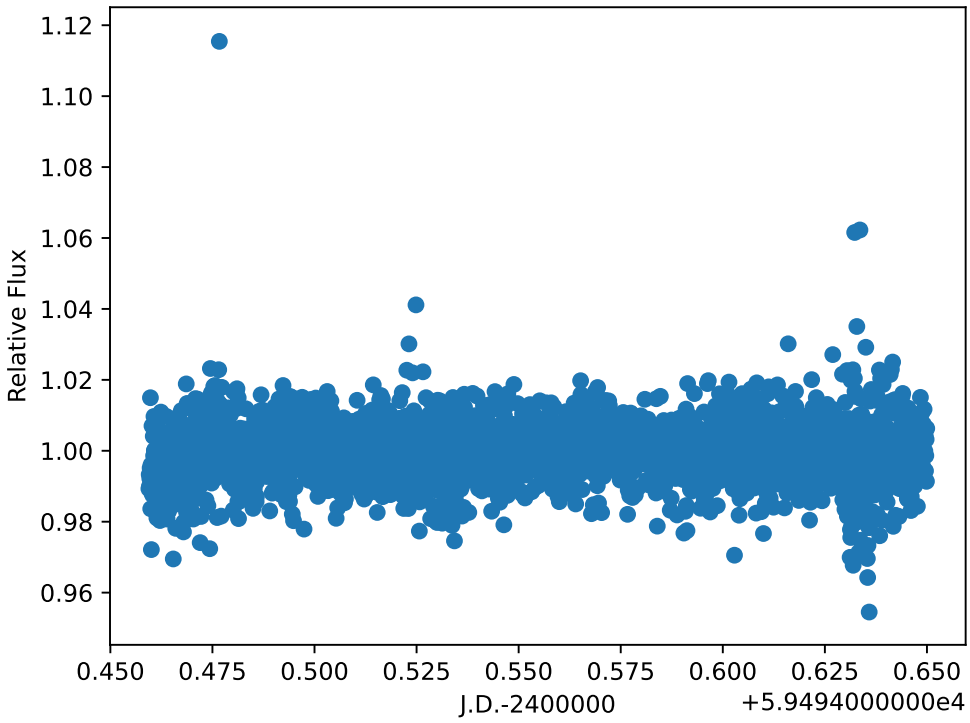

Figure 4.2: Unbinned relative flux over time of HD 206751 on the night of 2021 Oct 6.

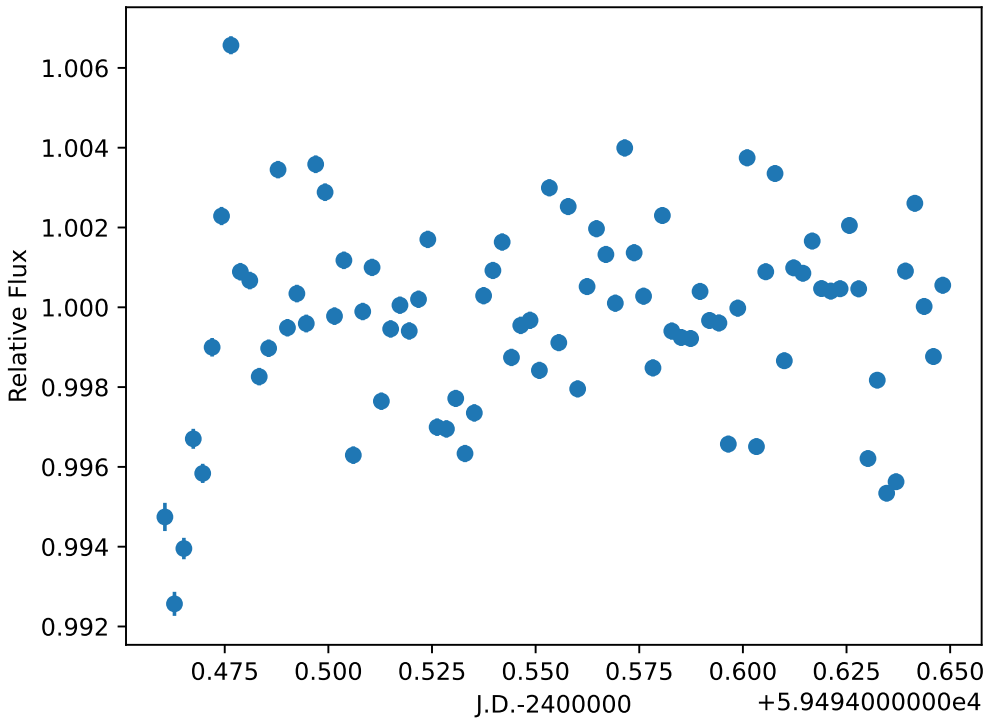

Figure 4.3: Relative flux over time of HD 206751 on the night of 2021 Oct 6 binned by 30 points.

indicates that there are intrinsic variations in the flux of the star on timescales of 5 bins or more that cannot be averaged out. The more flat the light curve, the longer it takes for the error to diverge from the standard deviation. As we will see in Chapter 5, HD 206751 has a particularly flat light curve so the other targets show a greater deviation between the standard deviation and error at lower bin sizes.

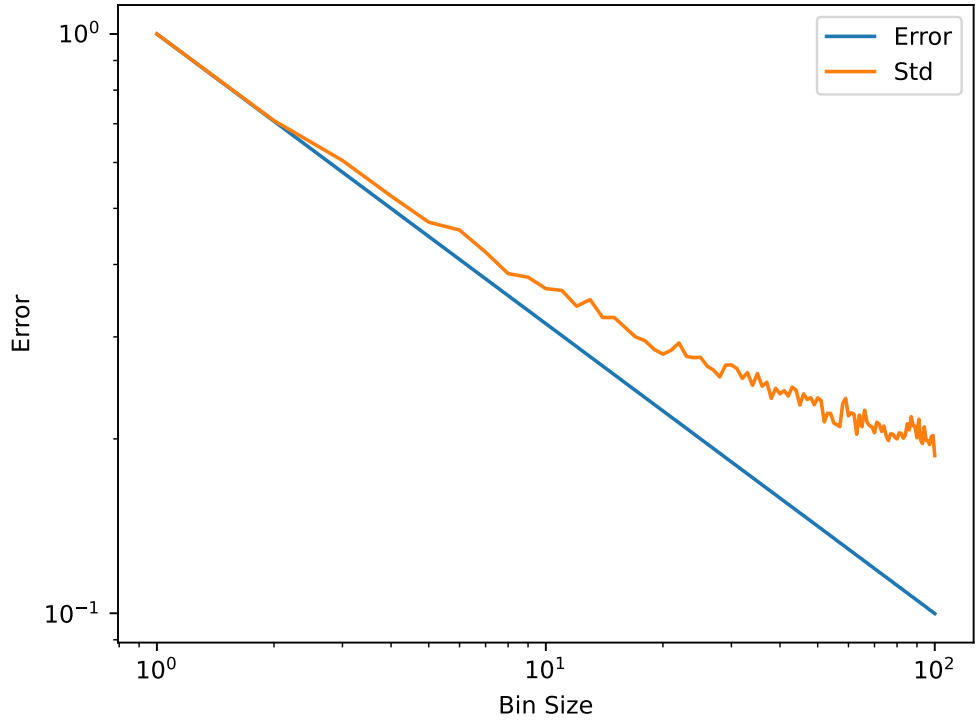

Figure 4.4: Error calculated from `AstroImageJ` compared to the standard deviation as a function of bin size for HD 206751 on the night of 2021 Oct 6. Both are normalized using the error and standard deviation before binning.

Variation in the flux of the target star can also be affected by the variation of one or more reference stars. To test for this possibility, I produce a diagnostic plot that graphs the brightness of the target star against the brightness of each reference star. The results for HD 206751 are displayed in Figure 4.5. If the

reference stars' flux remains constant for changes in the target stars flux, we know that the change in flux is in the reference star. If there is some slope to this relationship, a reference star may be undergoing a flux variation of its own.

Typically for these bright targets, there are fewer than a dozen reference stars that are bright enough to use. Each one of these stars must maintain nearly constant brightness over the course of observation so the data does not become influenced by external variability. I have not found significant variability in the reference stars I used for the early bright star observations but I was motivated to examine variable reference stars because of an observation I made when observing the transit of GJ 9827 b. Displayed in Figure 4.6 is a similar plot to Figure 4.5 for my observation of GJ 9827. We see that the reference star TYC 5244-1198-1 was greatly affecting the relative flux measurement of GJ 9827. For this reason, the reference star had to be thrown out and the new differential photometry without this reference star produced a much flatter light curve.

The final two plots generated by the diagnostic program look for issues in the telescope's pointing. One issue that was present before the implementation of automated dome tracking was vibrations from walking into the dome and manually aligning it likely caused residual vibrations that shake the telescope for a few minutes. This manifested in broadening the stars FWHM. As shown in Figure 4.7, on average the FWHM is larger after making a dome adjustment. After the dome tracking became automated, the observer no longer required direct in-person alignment of the dome and the FWHM no longer had this periodic variation. To ensure this remained the case, the diagnostic program plots the FWHM over time.

The FWHM of approximately 13 pixels displayed in Figure 4.7 is about twice as large as what can be achieved by putting the stars perfectly in focus. For the observations of these bright stars, I purposely defocused the image so the light

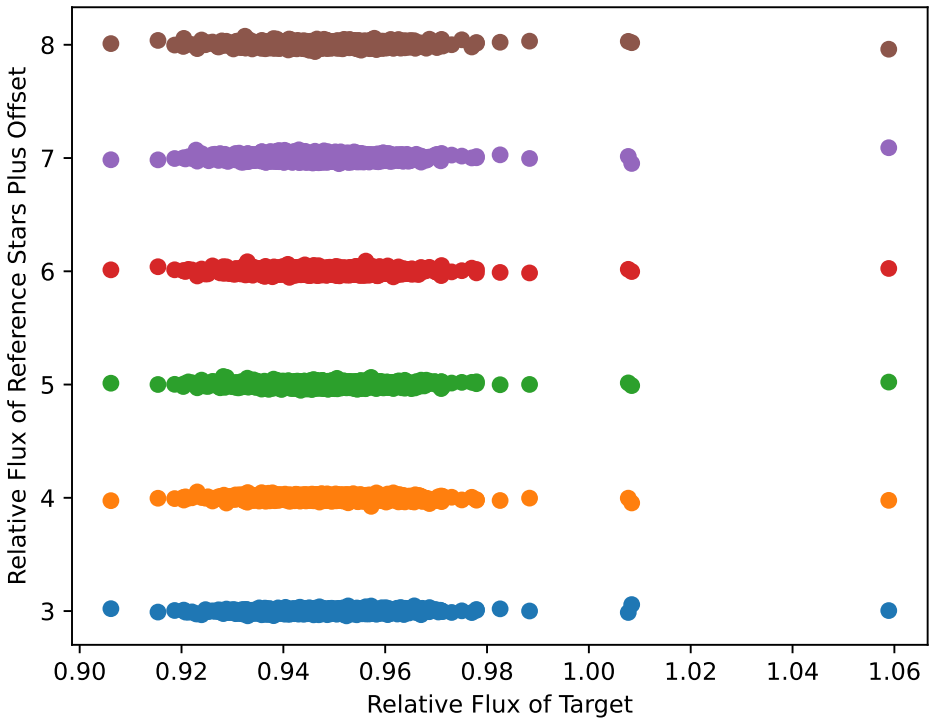

Figure 4.5: Comparing the relative flux of the target star to each reference star for each image of HD 206751 on the night of 2021 Oct 6.

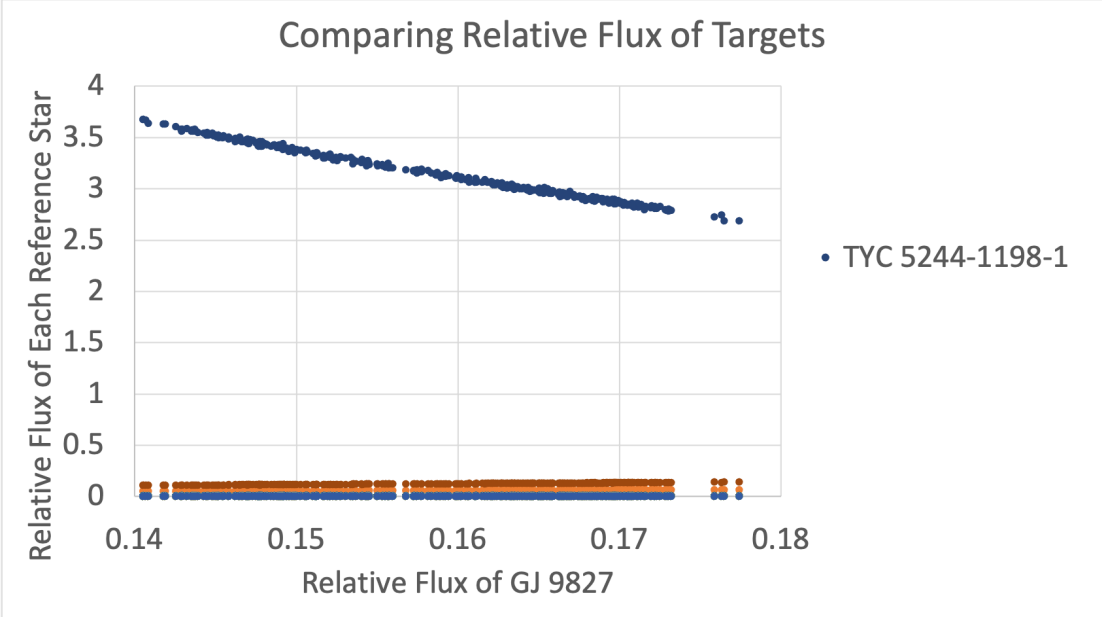

Figure 4.6: Comparing the relative flux of the target star to each reference star for each image of GJ 9827 on 2020 Nov 6. In this plot, we see the reference star TYC 5244-1198-1 changes dramatically with the measured relative flux of GJ 9827, meaning this reference star is too variable to use.

could be spread across more pixels, allowing for longer exposure times without reaching saturation. With too short exposures, the time it takes to read out the CCD will take up a greater percentage of observation time.

This issue of vibrations affecting the telescope's pointing may be a product of the alt-az mount. Unlike equatorially mounted telescopes which have one axis fixed along the direction of Earth's rotation, alt-az mounts have two axes that must be continuously adjusted when tracking a target. This could make an alt-az mounted telescope more vulnerable to vibrations because there is not the built-in tracking stability of equatorially mounted telescopes.

Another issue was in the pointing model of the telescope. Pointing the telescope solely with PlaneWave software caused the target to not remain centered over the course of an observing run. Paired with the initial rotator issues, this

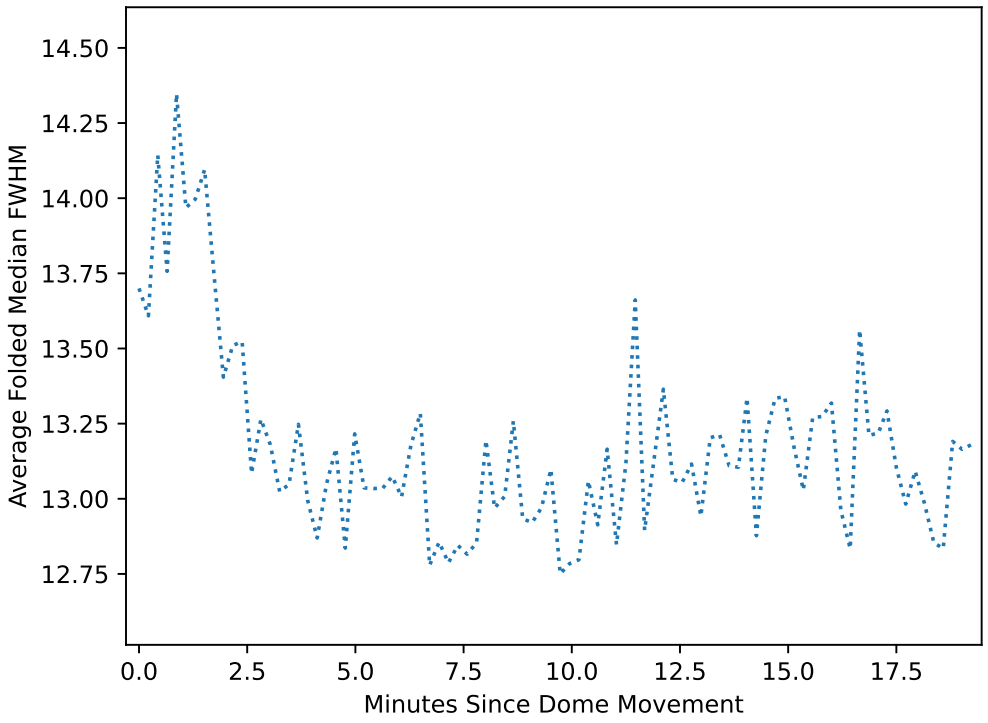

Figure 4.7: Averaging the FWHM measured in pixels folded over the time since dome adjustment.

caused dramatic motion of targets over the course of a night. Using ACP with its plate-solving abilities has corrected this issue. To monitor unexpected motions of targets throughout the night, a plot of the centroid position of the target star and reference stars is generated by the diagnostic program.

4.4 Minimum Detectable Exoplanet Radius

In order to find a precise estimate of the minimum detectable radius, we can simulate what a transit would look like in real data. To accomplish this injection, a transit model is generated using the transit modeling `Python` package `batman` created by Kreidberg (2015). To make an injection, this normalized model is multiplied by the raw data. Out-of-transit model data has a value of one while the in-transit data is some value less than one dependent on the planet to star ratio. The shape of the transit light curve is modeled using variables like semi-major amplitude, period, eccentricity, longitude of periastron and the limb darkening properties of the star. For the minimum detectable planet program, the parameter of interest was the planet to star radius ratio. An example transit I generated with `batman` is displayed in Figure 4.8.

To figure out if a planet transit could first be picked out of the data, I used a method called Box Least Squares (BLS) from the `Astropy Python` package created by Astropy Collaboration et al. (2018). This method attempts to model transits in the data using a basic box function displayed in Figure 4.9 that only has parameters of period, depth and transit midpoint time. By running through potential periods, phases and depths, the squared differences between the model and data are calculated. By minimizing the squares of the residuals, we find the most likely period, depth and time of transit.

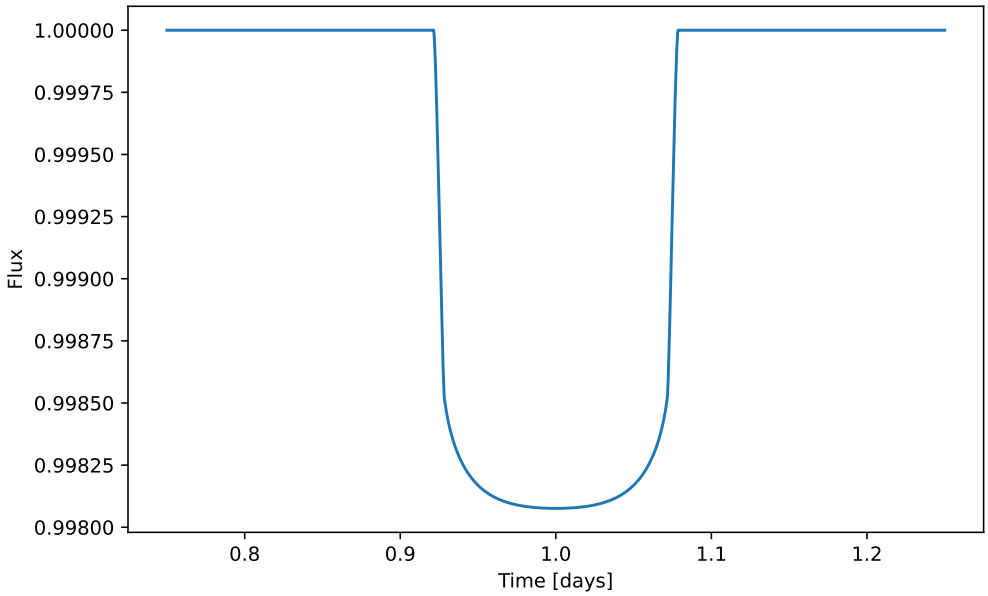

Figure 4.8: `Batman` transit model of Jupiter radius planet orbiting Vega at 0.025 au with a period of a day.

The minimum detectable planet program starts with a loop of the planet to star ratio of 0.1% and then increases this ratio by 0.1% for each iteration. At each iteration, a model is generated and injected into the data on the first night of observation, three hours from the start of observation. The relative flux outputted by `AstroImageJ` is not properly normalized so each night is normalized by dividing each point by the median value. The normalization is done after each injection to make the simulated data reduction the same as if a real transit was observed. Then, the BLS method is used to generate the highest likelihood time for the transit. If the potential transit found by the BLS method has a midpoint time within 14.4 minutes of the injected transit time, then the planet is identified as detected and the loop breaks. The 14.4-minute threshold was chosen because it represents 0.01 of a day. At this threshold, I found my program works best at

differentiating between detection and non-detection when comparing folded light curves with different thresholds of detection. The radius to star ratio at which the BLS method and the injected transit times align is the minimum detectable planet size. To turn this ratio into an absolute planetary radius, we can estimate the stellar radius given its temperature using Equation 3.6 derived in Section 3.4. Examples of injections I have made into my observations are discussed in Section 5.6.

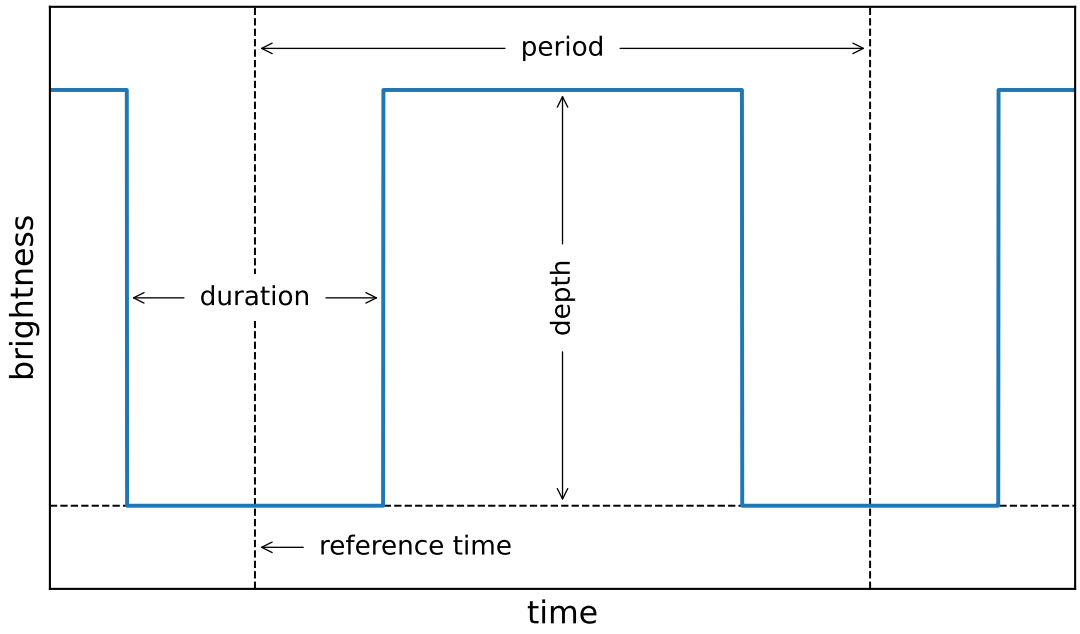

Figure 4.9: Figure from `Astropy` documentation created by Astropy Collaboration et al. (2018) depicts the box functions that are used to detect potential transits via the BLS method.

Injecting a transit into a single point in photometric data does not give us a complete view of the minimum planet we can detect because different sections of data have different levels of scattering and noise. To get a complete description of the likelihood of picking out a transit of a given radius, we need to inject a transit at many points in the data and determine the percent of detections made for each

radius planet. In the next section, I describe how I adapted my program to test the sensitivity across all points in my observations.

4.5 Phase Variable Detectability

By taking the minimum detectable radius program and putting it in a loop that varies the period of injection, we can test the performance of the BLS method across different locations in the data. For each target, there are different numbers of reference stars and different signal-to-noise ratios. Sky conditions also cause scattering that increases the standard deviation of data. Varying the location of an injected transit in the data, we can obtain a more accurate account for what size planet can be detected. Because I use real data to inject these transits into, these simulations describe the real limits of possible detections. If potential transits appear in the data with transit depths much smaller than what the injection code says we can detect, the transit is likely not real.

First, each night is normalized without any injection and the BLS function is run to find the point in the data where it believes there to be a transit. The point identified as a transit in the raw data must be skipped over when making an injection because BLS will mark an injection in that location as detected even if the injection is too small to detect. Once the injection produces a BLS model that has smaller residuals than the model produced from the flux variation present in the raw data, a detection can be identified.

Like in the minimum debatable radius program, a planet to star radius ratio is chosen. Again, I start with 0.1% and increase the ratio by 0.1% for each iteration. Then the phase of the injection is chosen. I use the 0.01 day (14.4 minutes) intervals as the tolerance and step size for phase shift. The first injection is

made with the midpoint occurring 14.4 minutes from the start of observation. BLS modeling is run and if the transit midpoint identified is within 14.4 of the injection midpoint, it is counted as detected. The phase is then shifted by 14.4 minutes and the detection process repeats. Once the injection midpoint is within 14.4 minutes of the end of that night of observation, the injection skips to the next night of observation using the same 14.4 minutes buffer. The phase is shifted until every night has been injected with a complete set of transits.

At the end of a set of each phase shift for a given radius of injection, the percent of phase shifts that were detected is calculated by dividing the number of detections by the number of phase shifts. Then the radius is increased by 0.1% and the phase variable detection process repeats. By the end of the run, we obtain the percent of detections made for each radius planet.

4.5.1 Probability of Transit Detection

The transit probability program uses the time intervals of observations to identify whether a transiting planet of a given period would transit during an observation. Because of the complexities and unique observing patterns of each target, I calculate directly the probability across different period planets from actual times of observation. Analytical calculations can be made as demonstrated by Burke & McCullough (2014). The equations in Burke & McCullough (2014) work best to estimate the probability trend after dozens of nights of observation with the same length of observation each night and do not capture the discontinuities in the probability distribution shown through numerical modeling.

The program takes an input of the start and end of observing times and outputs a list of planetary periods and their corresponding probability of detection.

Originally, I coded the program in `Python` but to improve the speed at which the calculations are made, I adapted the program to a lower-level language `C`. Especially for stars that were observed over many days, the probability can be calculated much more quickly in the `C` version.

The simulation is done by recording every interval where the telescope was observing. Then a hypothetical planet with a certain period and time of transit is compared to observing times. If the observing time overlaps with the transit time, it is marked as a detection. If the transit occurs when not observing, it is a non-detection. Then the process repeats by shifting the phase of the hypothetical transiting planet and seeing if a detection is made.

A simple example is if we think about a transiting planet with a period of a third of a day and we observe it for half a day, we are guaranteed to see it after just one observation because the transit will have to repeat within the observing window. If a transiting planet has a period of a day and we observe for half a day, the chance of seeing the transit drops to 50% because there is a 50-50 chance the transit happens at night or during the day. Figure 4.10 shows the probability distributions for different hours a night and different numbers of nights of observations. These curves are relatively smooth compared to the real simulation displayed in Section 5.7 which contains real times of observations with days between observations and varying lengths of observation. Probabilities become more difficult to calculate for erratic observing times which is why numerical simulation is the best way to make the calculation.

To get a distribution of detection probabilities as a function of period, the program is run for 100 periods up to 14 days. When the probability is at 100%, a planet of that period can be ruled out assuming it is large enough to be detected. Combining the results from this simulation and with the injection code, we can

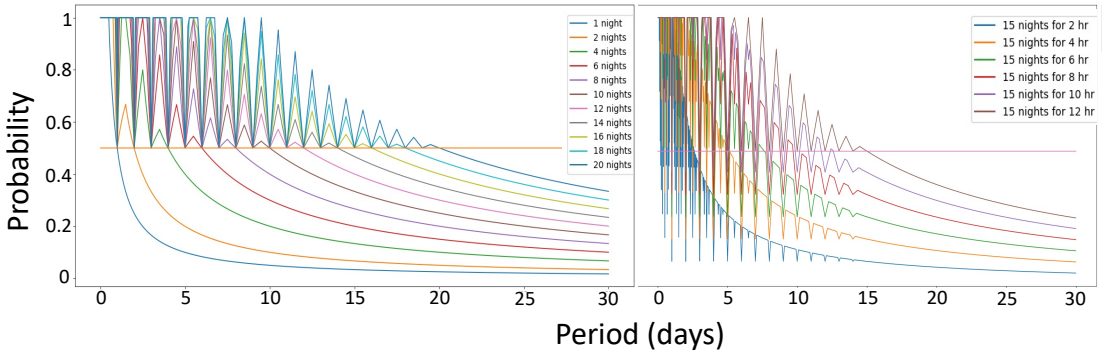

Figure 4.10: These plots show the probability associated with detecting a transiting exoplanet given the planet's period. The right plot displays probability distributions assuming ideal 12 hours a night consecutive observations with the legend specifying the number of nights. The left plot maintains a 15-night consecutive observing program but each line represents a different number of nightly hours a target is observed. Horizontal lines mark 50% probability.

rule out short-period planets above the radius threshold. We can also decide how long to spend on a target through these simulations by choosing a probability threshold for detecting a certain period planet. For example, for each target, we might want to reach an 80% probability of detecting a 3-day period transiting planet. Using this numerical simulation, we are given a clear picture of what transiting planets have been ruled out and if the probability of detecting longer period planets is high enough to justify further observations.

Chapter 5

Results

Starting in the fall of 2022, observations using Van Vleck Observatory's Plane-Wave 24-inch telescope were taken on most clear nights. This section discusses the preliminary results of this pilot study for four targets. As observations continue, data will be continually reduced and the data analysis pipeline described in Section 4 can be efficiently applied. As the telescope's functionality nears full automation, observations can be obtained with greater frequency and for longer periods of time, increasing the probability of detection.

5.1 Target Stars

Using the target acquisition program described in Section 2.2, I hand-selected targets in my sample that met ideal observing conditions so that precise photometric measurements could be obtained. The properties of these stars are outlined in Table 5.1. All the stars in this initial sample are main sequence F-type stars because they are still within the brightness-temperature range of stars that lack exoplanet detections but their smaller radius allows for the detection of smaller exoplanets. All stars with available $v \sin i$ data were chosen to be near the upper limit of rotational speed to potentially increase the probability that $i = 90$. Table 5.2 describes some of the details of the observations made of each object.

Name	**RA [hr:min:sec]**	**Dec [deg:min:sec]**	**B mag**	**Spectral Type**	**T_{eff} [K]**	**$v \sin i$ [km/s]**
HD 32715	05:09:44.506	+64:55:10.163	6.770	F3V	6615	42.0
HD 206751	21:44:07.922	+07:09:29.723	7.81	F2V	6612	...
HD 6314	01:04:36.449	+39:59:27.995	7.074	F0Vn	7129	165
HD 21844	03:33:20.973	+47:57:00.293	6.91	F1V	6816	...

Table 5.1: Stellar parameters of each target using data latest data from SIMBAD (Wenger et al. 2000).

Name	**Hours**	**Images**	**Exposure Time [s]**	**Median Standard Deviation**	**Relative Flux SNR**
HD 32715	11.34	8001	1	4.30%	77.43
HD 206751	24.69	13830	2.5	1.10%	850.5
HD 6314	58.56	32045	0.8	3.77%	381.9
HD 21844	34.74	14025	0.8	2.23%	310.1

Table 5.2: Length and parameters of observation for each target and the resulting photometric precision. The median standard deviation is calculated by finding the standard deviation of all relative flux measurements for each night and taking the median across all nights.

5.2 Light Curves

5.2.1 HD 32715

Each target was observed for varying periods of time and intervals between observations. HD 32715 was only observed for three nights and served as a good initial test of the telescope controls and data reduction. The target was observed on three consecutive nights from 2021 Sep 18 to 2021 Sep 20. The entire light curve is displayed in Figure 5.1. The errors on the first night of observation are much larger because I did not take calibration images for that night.

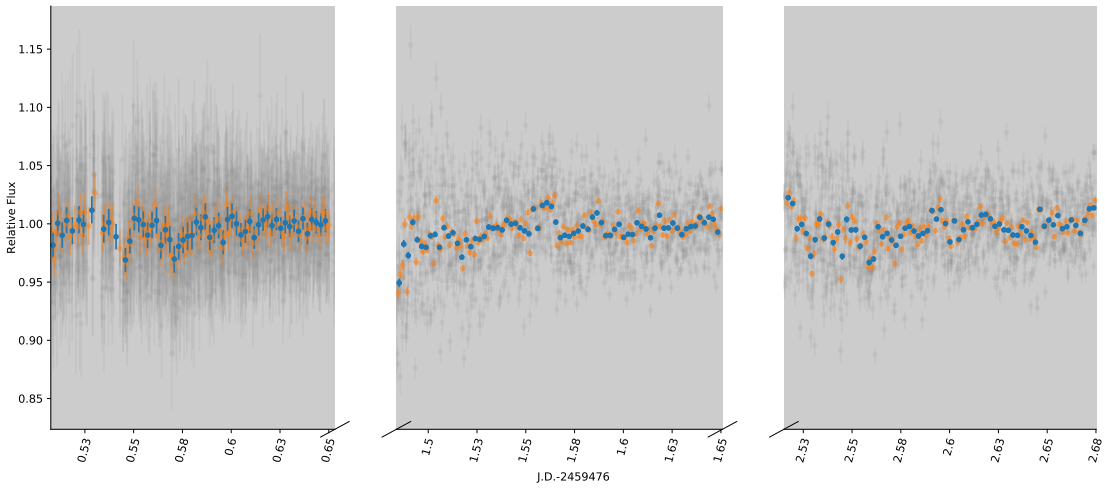

Figure 5.1: Light curve for HD 32715 from 2021 Sep 18 to 2021 Sep 20. The gray points are unbinned data. The orange and blue points are the same data in 20 and 40-point bins respectively.

The observations of HD 32715 had a high median standard deviation of 4.3% meaning the variations in the data may be noise rather than changes in flux from the star or transiting planet. The reason for this noise was most likely due to atmospheric scattering which can dominate the scattering of even bright targets (Osborn et al. 2015). When reference stars are dimmer, they become less reliable

at correcting atmospheric conditions that affect the entire field of view. We see from the field of view of HD 32715 displayed in Figure 5.2 that there is a lack of bright reference stars relative to the target. This yielded a median relative flux signal to noise measurement of just 77 (see Table 5.2). In Section 5.3, I run the light through the BLS program to identify potential transit locations along with the strength of the BLS fit.

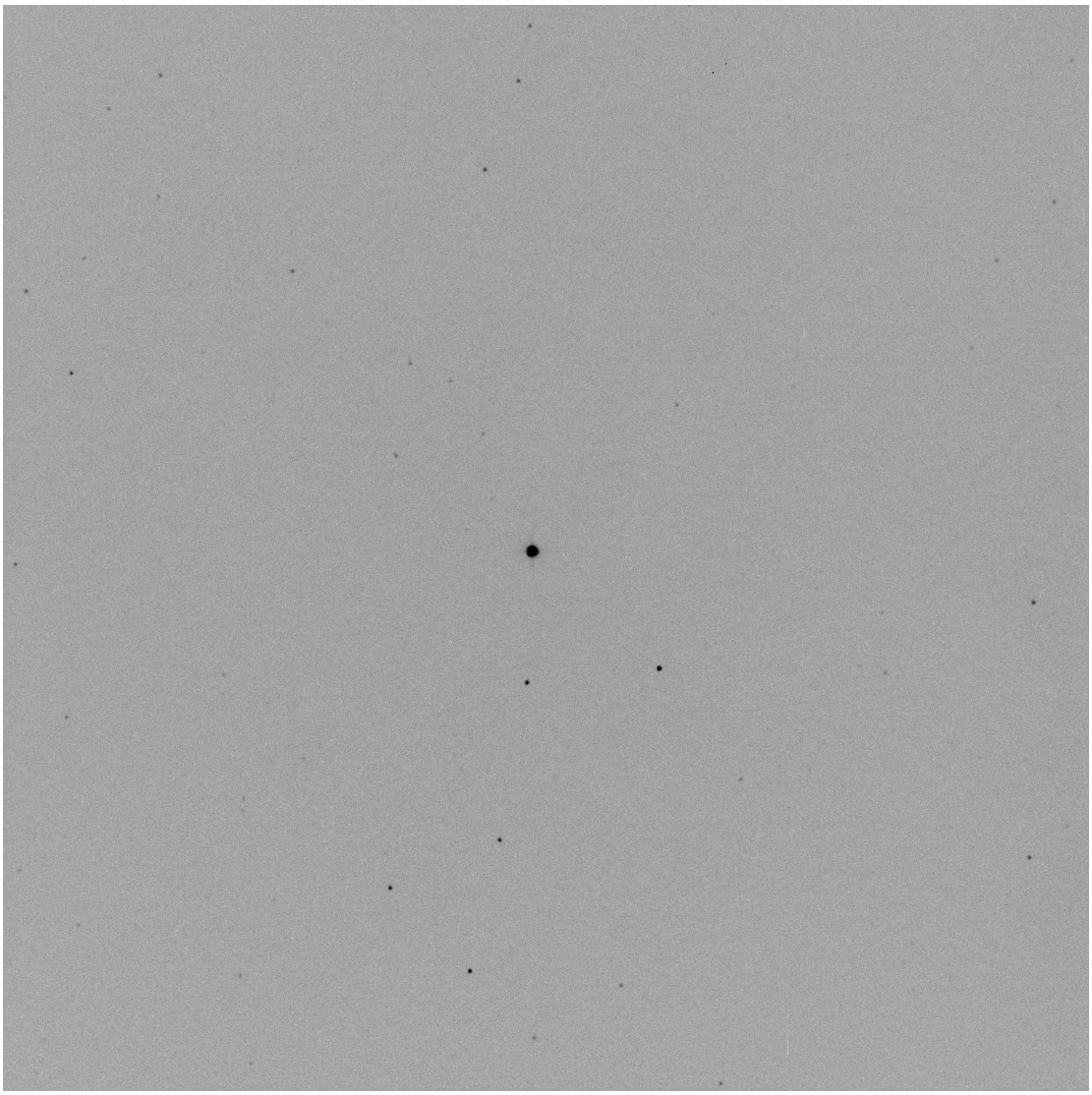

Figure 5.2: Negative image showing the field of view for HD 32715 (brightest star at center of image) taken through the PlaneWave 24-inch telescope.

5.2.2 HD 206751

The next target I observed was HD 206751 from 2021 Oct 2 to 2021 Oct 19. I observed HD 206751 for six nights and obtained much more precise data than I did for HD 32715. The standard deviation of the unbinned data was 1.1%. Looking at the light curve in Figure 5.3 we can see there do not seem to be significant variations in flux. On the second to last night of observation on 2021 Oct 18, I was not able to obtain continuous data due to intermittent clouds. On 2021 Oct 19, the final night of observation, I observed HD 206751 too long into the night and the atmosphere had a particularly strong scattering effect this night. As we can see there is a steady increase in scattering this night as the star reached a lower altitude.

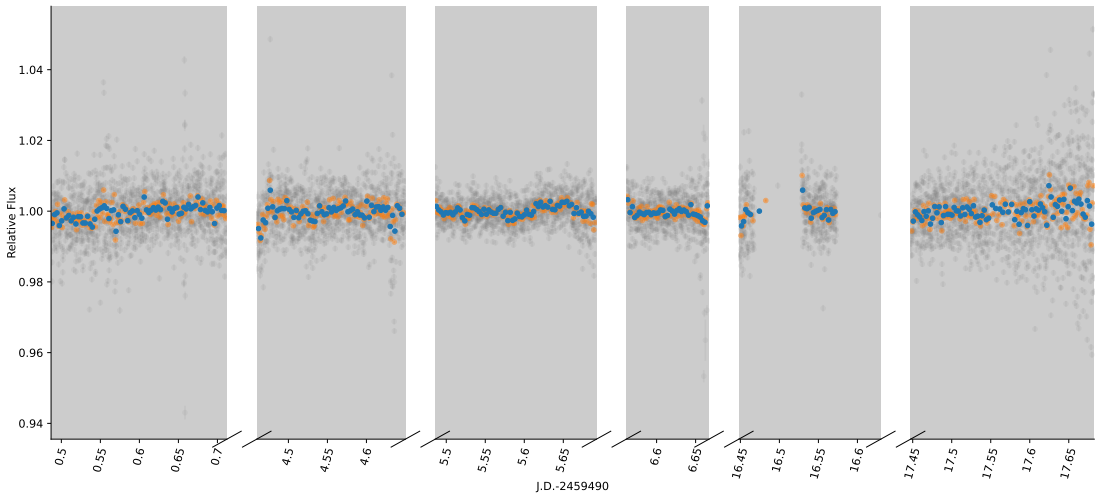

Figure 5.3: Light curve for HD 206751 from 2021 Oct 2 to 2021 Oct 19. The gray points are unbinned data. The orange and blue points are the same data in 20 and 40-point bins respectively.

Looking at Figure 5.4, we see that the number of bright reference stars is much higher for HD 206751 compared with HD 32715 displayed in Figure 5.2. Bright reference stars reduce the photometric noise and contribute to the lower error

bars and standard deviation visible in the light curve. With these observations, I obtained the highest relative flux SNR of 850.5.

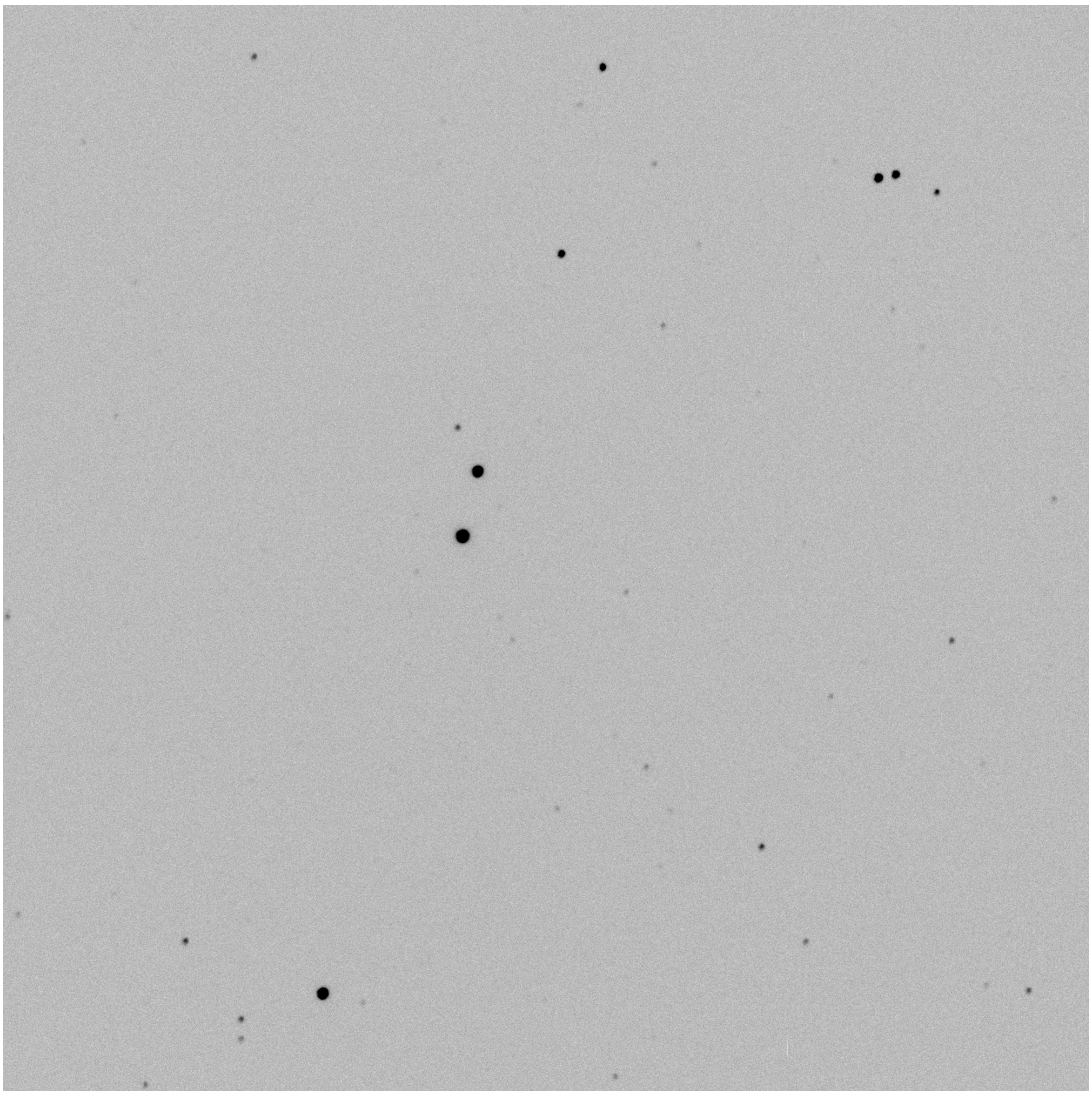

Figure 5.4: Negative image showing the field of view for HD 206751 (brightest star near the center of image) taken through the PlaneWave 24-inch telescope.

5.2.3 HD 6314

I have processed 12 nights of data for HD 6314 for observations beginning on 2021 Oct 29 and ending on 2022 Jan 8. In Figure 5.5, the field of view for

observations of HD 6314 shows plenty of bright reference stars, producing a relative flux SNR of 381.9. The data from HD 6314 shows extreme variability, making the BLS method ineffective at finding planetary transits. The star's brightness dropped by almost 25% from its initial brightness. This result demonstrates the potential of this survey to make discoveries beyond exoplanets in areas of stellar variability and pulsations. HD 6314 can be further studied to assess the type of variability present and analyze periodic patterns present in the light curve. The preliminary analysis of the light curve displayed in Figure 5.6 is discussed in Section 5.4.

5.2.4 HD 21844

I have processed seven nights of observations of HD 21844 beginning on 2022 Jan 15 and ending on 2022 Jan 31. There are some interesting variations in flux in these observations. It is challenging to determine if they are caused by stellar variability, atmospheric effects or planetary transits. Figure 5.7 displays the light curve for these six nights. In Section 5.3, I use the BLS program to examine the most likely transit locations and model the planetary parameters.

5.3 Potential Transits

To pick out locations of potential transits, the Box Least Squares program was implemented to scan the observations of each target to identify the most probable location of a transit. First, we will examine our first target, HD 32715. The BLS method generates a periodogram which displays the quality of the fit as a function of period. A good measure of the quality of the fit is the parameter depth S/N which compares the depth of the fitted transit to noise found in the data. The

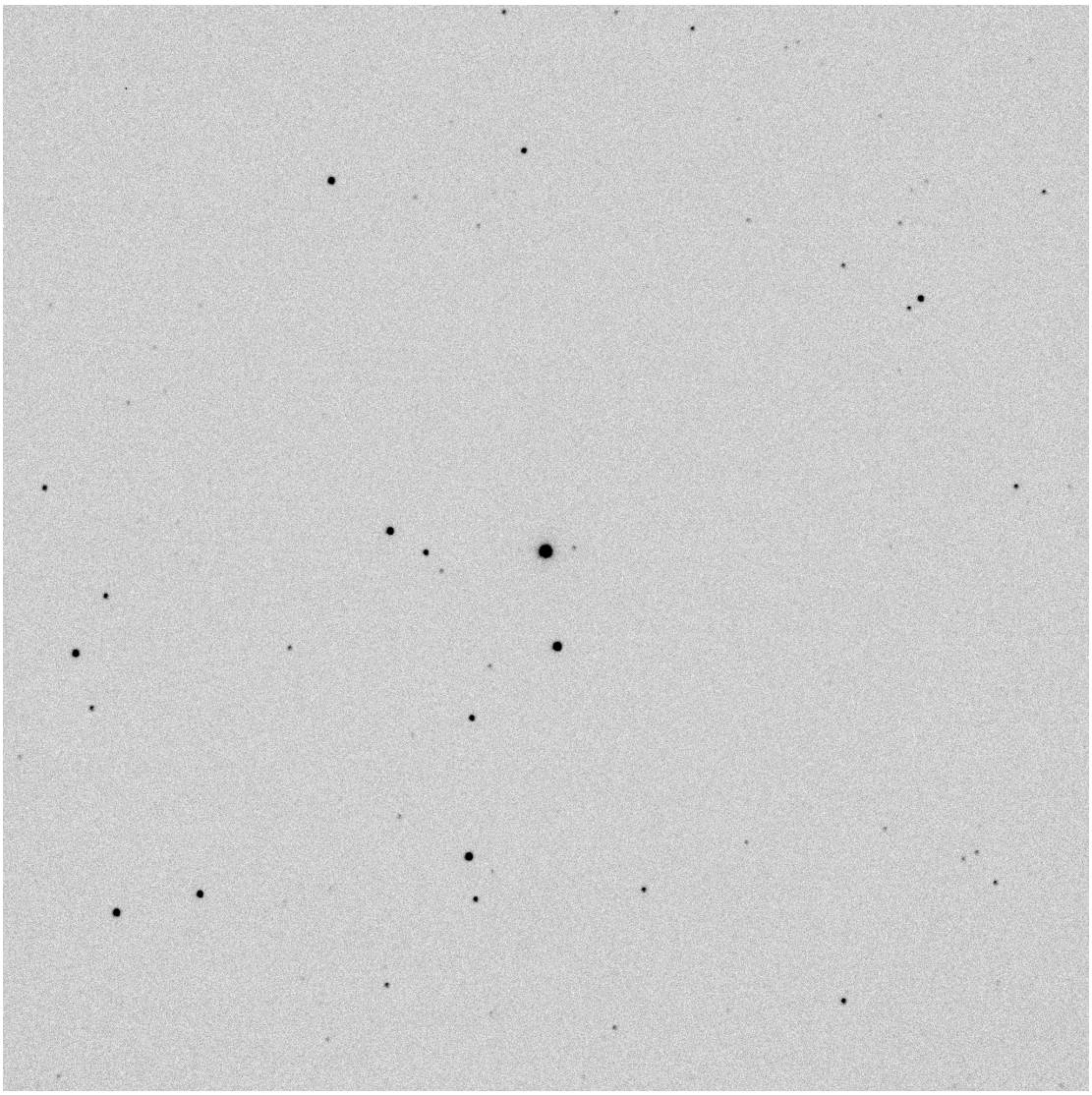

Figure 5.5: Negative image showing the field of view for HD 6314 (brightest star near the center of image) taken through the PlaneWave 24-inch telescope.

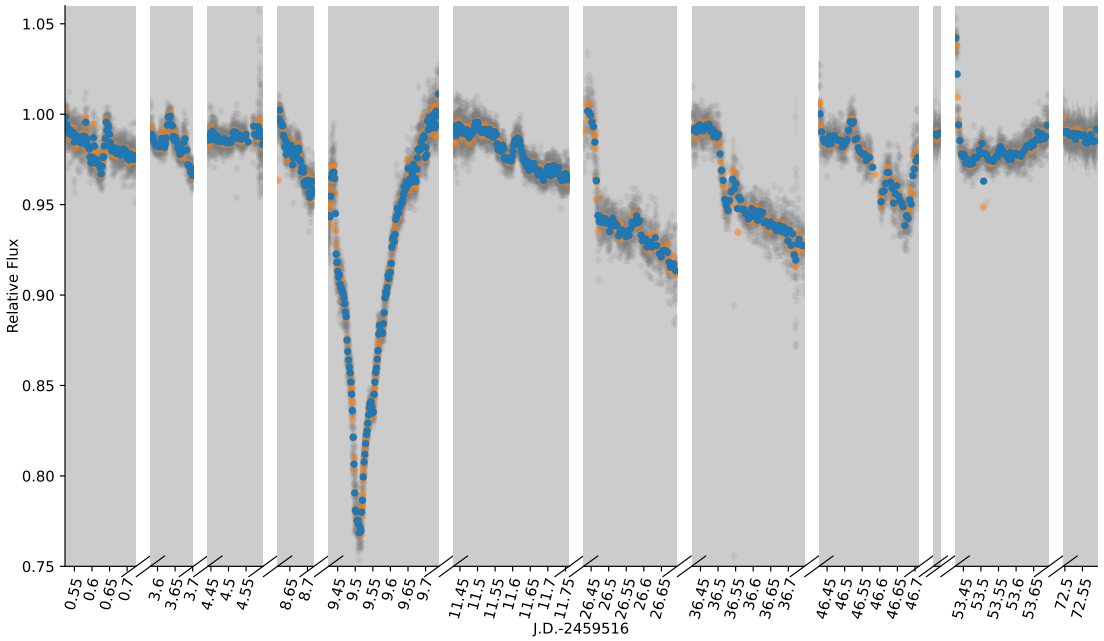

Figure 5.6: Light curve for HD 6314 from 2021 Oct 29 to 2022 Jan 8. The gray points are unbinned data. The orange and blue points are the same data in 20 and 40-point bins respectively.

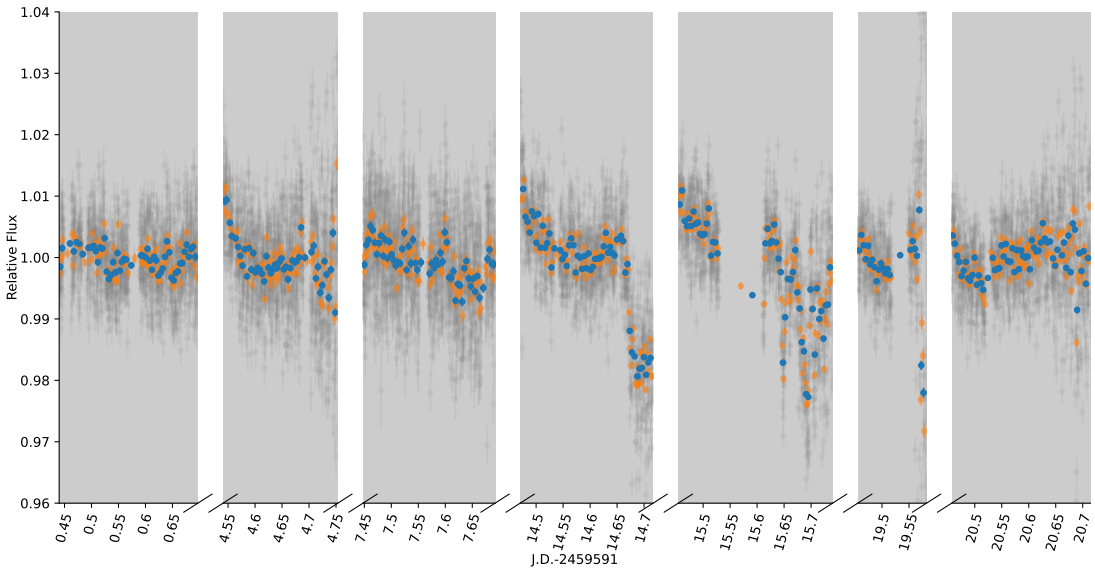

Figure 5.7: Light curve for HD 21844 from 2022 Jan 15 to 2022 Jan 31. The gray points are unbinned data. The orange and blue points are the same data in 20 and 40-point bins respectively. On the fourth night, there appears to be transit-like behavior in the light curve.

periodogram for HD 32715 is displayed in Figure 5.8.

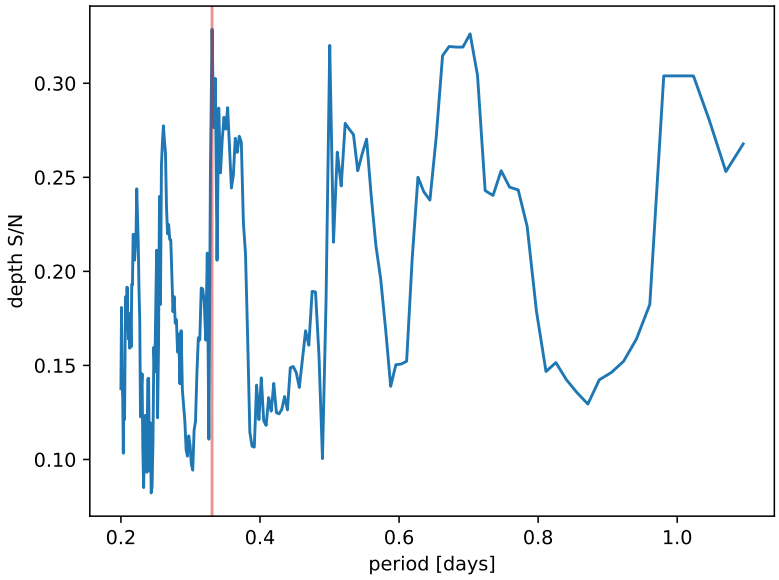

Figure 5.8: BLS periodogram for HD 32715. Highest depth S/N period is at 0.33 days (marked by red vertical line).

We see from this graph that the depth S/N is very low for any given period. When we chose the best fit we see that the best location for a transit is found where no data was taken. The best fit period is 0.33 days. Figure 5.9 displays the data folded over the transit time that was selected at the given period. From this result, it is clear that no transit is detectable in this data.

Running the HD 206751 data through the BLS program we see once again the best fit is found where no data exists, indicating no full transit was detected. Figure 5.10 shows the depth S/N remains low across potential fits, under half that of HD 32715. Figure 5.11 displays the lack of data in the region the transit was predicted. The transit time picked out is closest to the first day so I attempted to model a transit light curve during that night in Section 5.5.

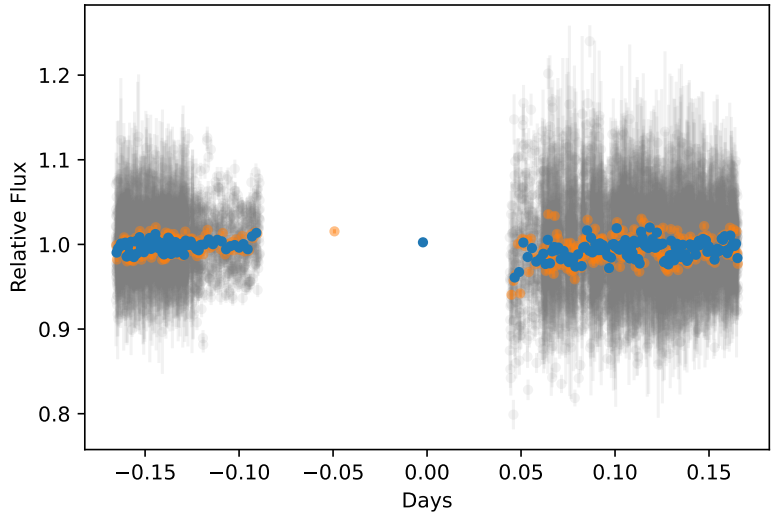

Figure 5.9: Folded light curve of HD 32715 using BLS derived period of 0.33 days. The gray points are unbinned data. The orange and blue points are the same data in 20 and 40-point bins respectively. The two points in the middle are an effect of the binning where points at the edges of either observing run were binned together. No observations were made in the region the transit is predicted.

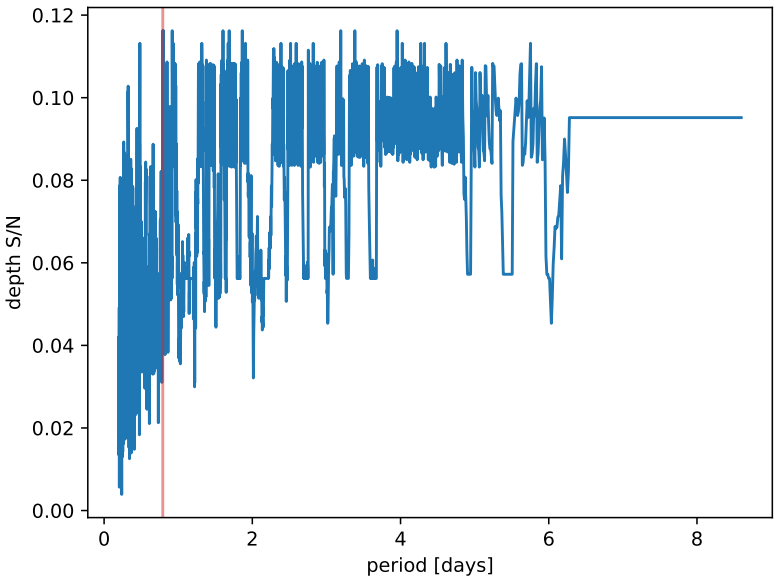

Figure 5.10: BLS periodogram for HD 206751. Highest depth S/N period is at 0.79 days (marked by red vertical line).

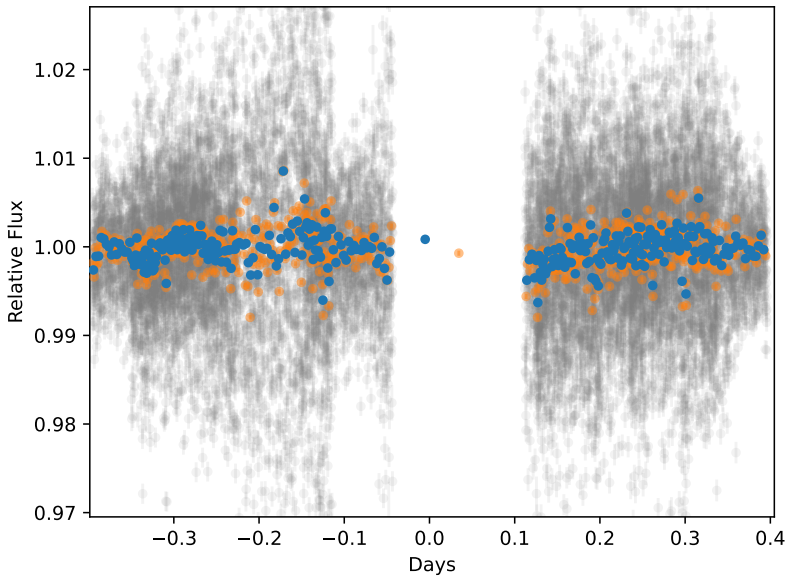

Figure 5.11: Folded light curve of HD 206751 using BLS derived period of 0.79 days. The gray points are unbinned data. The orange and blue points are the same data in 20 and 40-point bins respectively.

5.4 Variability in the HD 6314 Light Curve

HD 6314 displayed extreme variability as shown in Figure 5.6. Particularly on the night of 2021 Nov 6 where there is a nearly 25% drop in the relative flux of HD 6314. While variable stars or potential eclipsing binary stars are not the focus of this study, the outcome of these observations demonstrates other discoveries beyond exoplanets that can be made with these observations.

The spectral type of HD 6314 is a F0Vn type star with the "n" indicating broad absorption lines indicative of fast rotation. This is expected due to the star's relatively high $v \sin i$ of 165 (Royer et al. 2007). Looking into the studies of HD 6314, it has been identified by Kervella et al. (2019) with *Gaia* and *Hipparcos* to be among 117,222 objects with a stellar and/or substellar companion. The main

star was found to have a mass of 1.699 $M_\odot$ with a 0.2183 $M_\odot$ companion (Kervella et al. 2019). If this star system is an eclipsing binary star system, perhaps this could explain the major drop in brightness.

Assuming that the densities of the two stars are the same, I can estimate what the transit depth will be in terms of mass: $\delta = (M_1/M_2)^{2/3} = (0.2183/1.699)^{2/3} = 25.5\%$. The fact that this is approximately the transit depth observed on 2021 Nov 6 indicates this system could be an eclipsing binary.

Looking at the night with the major drop in relative flux more closely in Figure 5.12 we see that the light curve is asymmetric which I would not expect for an eclipsing binary star system. There is also the presence of smaller oscillations along the light curve. In Figure 5.13, we can see an example of this smaller oscillation on the night of 2021 Nov 7. All these variability patterns must be studied in more detail to determine their source. Possible explanations include starspots which change the apparent flux as the star rapidly rotates, an eclipsing binary and stellar pulsations which cause a periodic change in luminosity.

5.5 Transit Modeling

To model potential transits, I used the `batman` package created by Kreidberg (2015) along with the SciPy `curve_fit` package created by Virtanen et al. (2020). By creating a function that creates a `batman` transit model, I can call the SciPy `curve_fit` routine to fit the best possible transit to the data by limiting the squared difference between the real data and model data. SciPy `curve_fit` then returns the planetary parameters that produced the best fit along with the error associated with the fit based on each apparent flux measurement and the degree to which varying a parameter affects the fit. For example, if I am modeling a

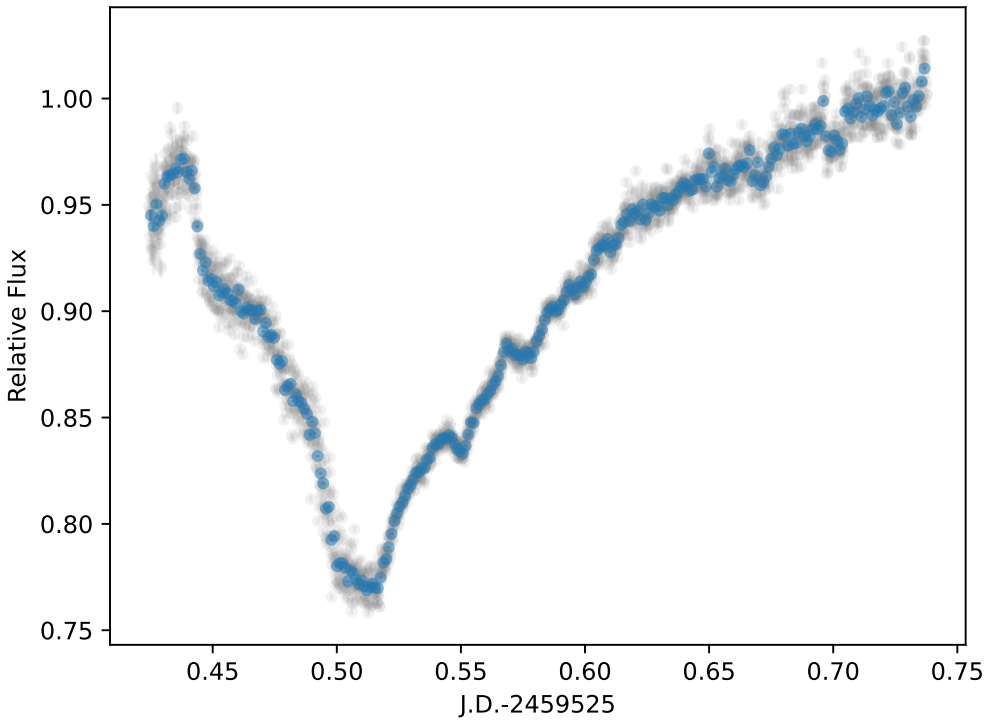

Figure 5.12: Light curve for HD 6314 on 2021 Nov 6. The gray points are unbinned data. The blue points are the same data in 20-point bins.

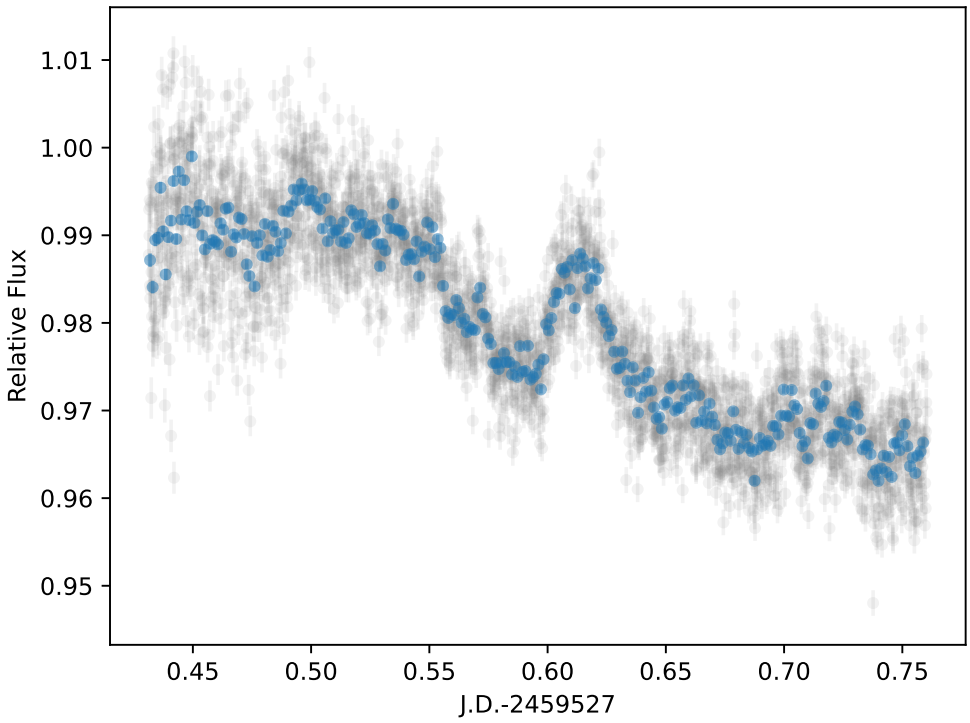

Figure 5.13: Light curve for HD 6314 on 2021 Nov 7. The gray points are unbinned data. The blue points are the same data in 20-point bins.

single transit, the period parameter will have a large error because the period of the planet can vary quite a bit without a second transit detection. Combined with a tunable semimajor axis parameter, the transit light curve can be made to look very similar for different period-semimajor axis combinations. For future work, a full Markov Chain Monte Carlo fitting program will be used to get a better handle on the errors. For the purpose of the initial analysis of the data, the transit depth and time of inferior conjunctions have reasonable errors and can be used to get a handle on the basic planetary properties.

Modeling a potential partial transit of HD 206751 located at the beginning of observations on 2021 Oct 2, I obtained the fit displayed in Figure 5.14. The parameters of the fit displayed in the figure have absurdly large errors, except for the transit time and star to planet ratio. Using Equation 3.6 and the temperature of the star, the planet to star ratio of 0.048 ± 0.023 implies a planet of $R_p \approx$ 6.7 Earth radii. We certainly cannot determine if this slight variation in flux is evidence of a planet because the transit is shallow, incomplete and the fit is uncertain. While the modeling of HD 206751 data does not show the presence of a planet, it demonstrates the transit fitting process that can be employed for future potential transits.

When modeled through the BLS program, the most likely transit location for HD 21844 is once again a partial transit displayed in Figure 5.16. Note the heavily scattered points leading up to the transit identified from the BLS method. The cause of the abrupt scattering is likely caused by a cloud passing through the field of view. However, this feature is only present in the folded graph given the period chosen by the BLS method. Since the BLS method only detected a single transit, this period measurement does not have much meaning and the raw data from the night the transit occurs is used for modeling rather than the folded data. It

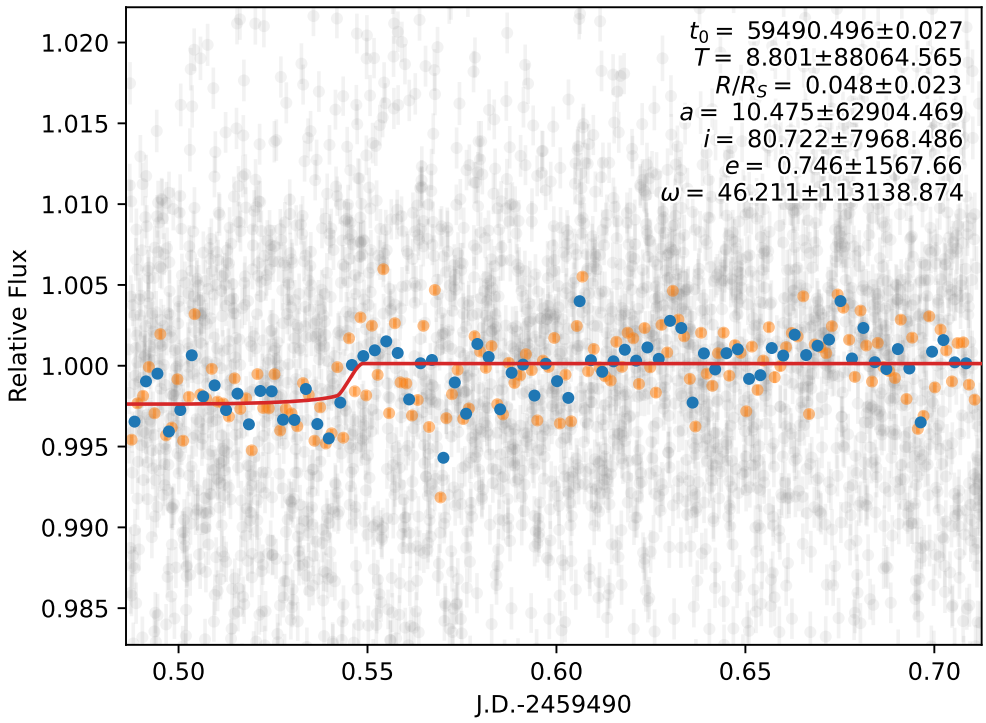

Figure 5.14: Transit of HD 206751 model. The gray points are unbinned data. The orange and blue points are the same data in 20 and 40-point bins respectively.

occurred on 2022 Jan 25 towards the end of observation. The model implies a 1.7 Jupiter radius-sized planet. Figure 5.17 displays this fit.

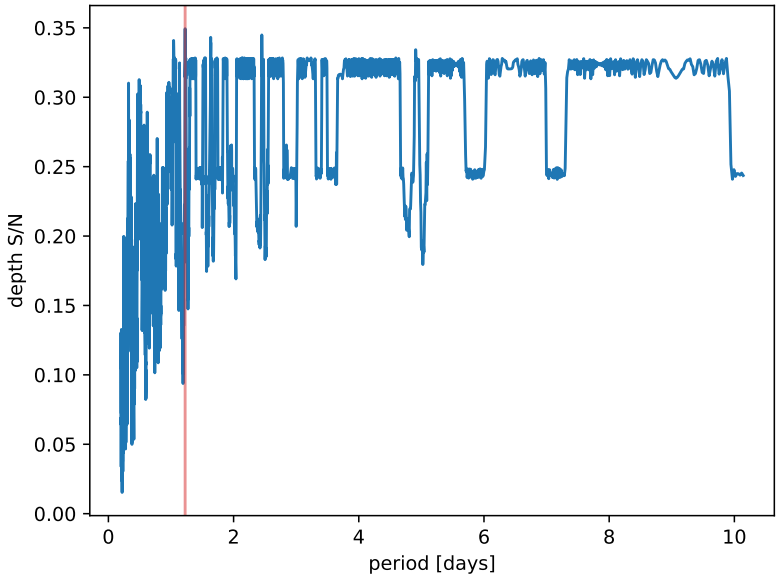

Figure 5.15: BLS periodogram for HD 21844. Highest depth S/N period is at 1.2 days (marked by red vertical line).

Looking back at the total light curve for HD 21844 displayed in Figure 5.7, we can identify a second but more scattered drop in flux on the second night of observation occurring on the night following the first potential transit on 2022 Jan 26. Since the transit is at a similar depth, I attempt to fit the transit curve with the same parameters as the 2022 Jan 25 fit to derive a transit time.

We see in Figure 5.18 that the drop in flux has a v-shape that prevents a good fit from being applied. The error for the time of inferior conjunction t_0 cannot be calculated because the bounds of the fit had to be made too narrow to force the model to fit the light curve. Regardless, analyzing the period derived from these models will test the process of analyzing the presence of multiple transit observations. To find the period, we simply find the difference between the two

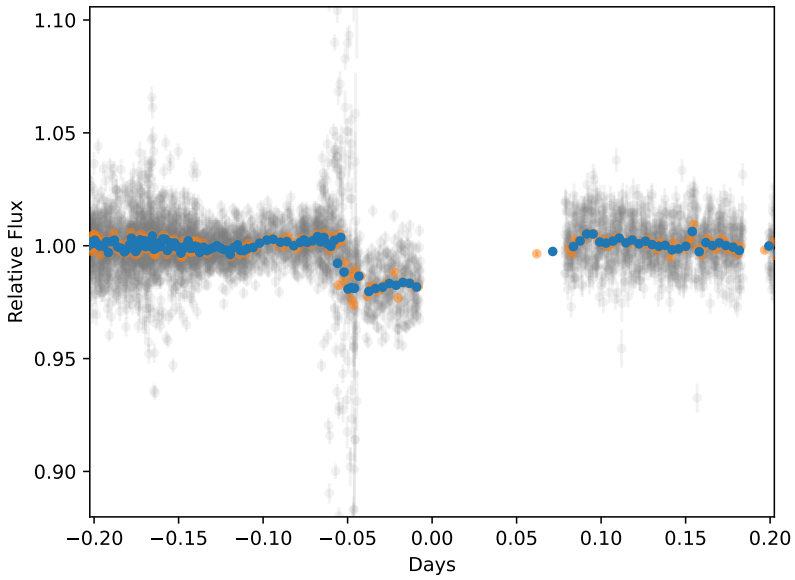

Figure 5.16: Folded light curve of HD 21844 using BLS derived period of 1.2 days. The gray points are unbinned data. The orange and blue points are the same data in 20 and 40-point bins respectively.

values of inferior conjunction derived from the models to get 0.96 days. I also estimated a second potential period using a t_0 of JD 2459606.7, the point where the relative flux is minimized on 2022 Jan 26. This yields a period of 1.001 days.

Using the initial transit time found on 2022 Jan 25 and the two period estimates using the second potential transit on 2022 Jan 26, we can examine the points in the light curve where we would expect other transits to occur. In Figure 5.19, I plot the total light curve of HD 21844 and mark the points with vertical lines where we would expect transits for the two period estimates. The 0.96-day period positions are marked in red and the 1.001-day period positions are marked in green. The points where the period estimates predict other transits do not show transiting exoplanets at those points. A closer examination of the light curve feature in Figure 5.18 shows the flux variation on 2022 Jan 26 does not have

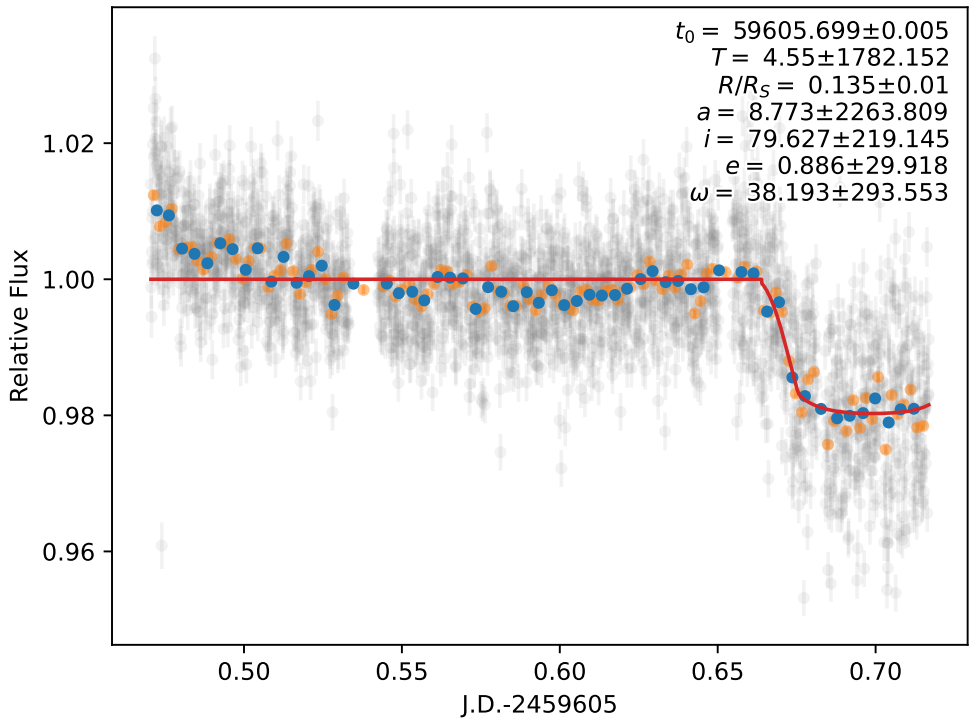

Figure 5.17: Transit of HD 21844 model on 2022 Jan 25. The gray points are unbinned data. The orange and blue points are the same data in 20 and 40-point bins respectively.

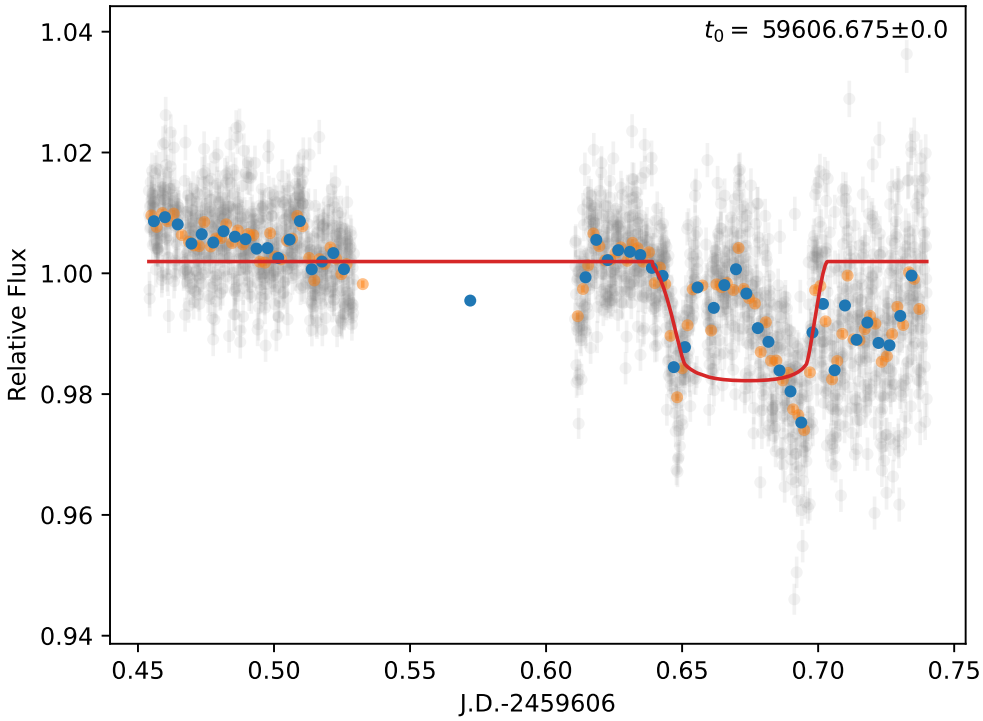

Figure 5.18: Transit of HD 21844 model on 2022 Jan 26 using the same parameters as the potential transit on 2022 Jan 25. The gray points are unbinned data. The orange and blue points are the same data in 20 and 40-point bins respectively.

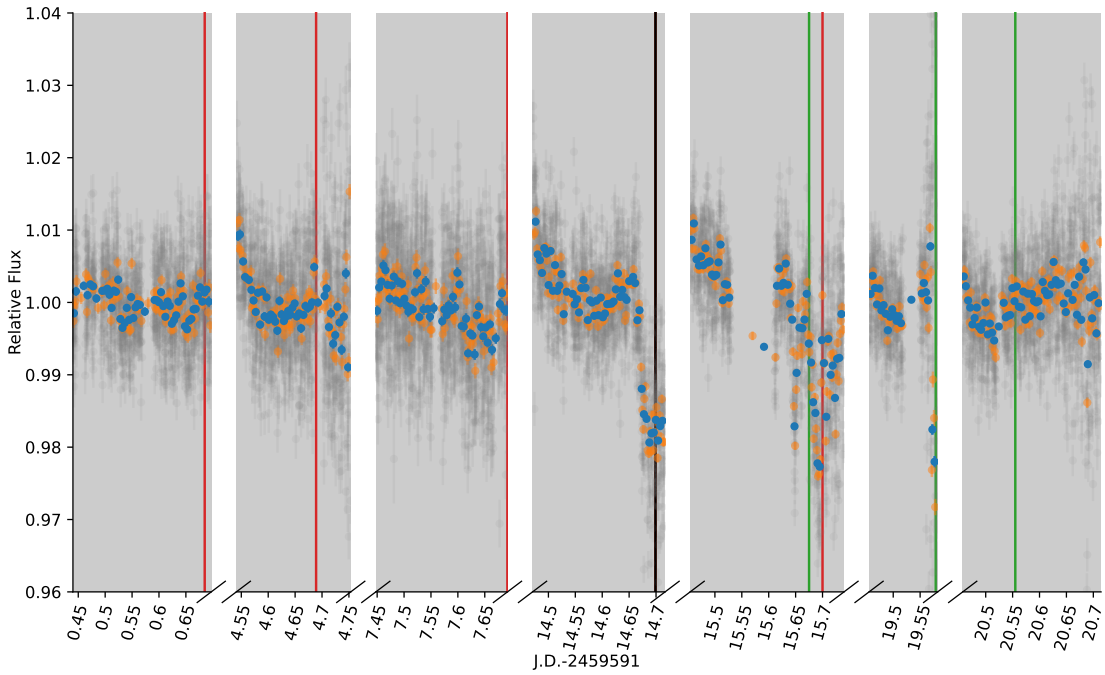

Figure 5.19: Light curve for HD 32715 starting on 2022 Jan 15. The gray points are unbinned data. The orange and blue points are the same data in 20 and 40-point bins respectively. Using the two period estimates, 0.96 days (green) and 1.001 days (green), I marked the locations with colored vertical lines where other transits would be expected assuming the transit on fourth night (black) occurred for both at the same time.

a transit-like shape so it is likely not a transit. In the future, this technique can be used to discover multiple transits within a light curve.

5.6 Detection Sensitivity

In this section, I will describe the results of using injections of model transits with `Batman` and the BLS method to determine what size planet this survey is sensitive to. I used the minimal detectable radius program described in Section 4.4 to get an initial estimate and the phase variable detection program described in Section 4.5 to get a more complete view of what can be detected across all possible transit locations in my data.

The data for HD 32715 had high levels of noise making it particularly difficult to pick out an injected transit. Using the minimum detectable radius program, the threshold required for a detection was about 4.3 Jupiter radii. The injected transit became so large that its transit duration ended up not fitting in a single night of observation. The resulting light curve with the injected transit overlayed is displayed in Figure 5.20. We see from this figure the data is centered around the model at the point of transit because the BLS method is attempting to fold non-transiting data over the injected location. The data collected for HD 32715, particularly on the first day where this transit was injected, is too noisy to detect sub-Jupiter-sized exoplanets.

HD 6314 is not suitable for running this program because the extreme variability of the star makes a transit injection of any size impossible to pick out via the BLS method. HD 206751 and HD 21844 produce more reasonable injection results because their light curves are relatively constant except for nights where potential transits were detected. For the purpose of injection, observations from

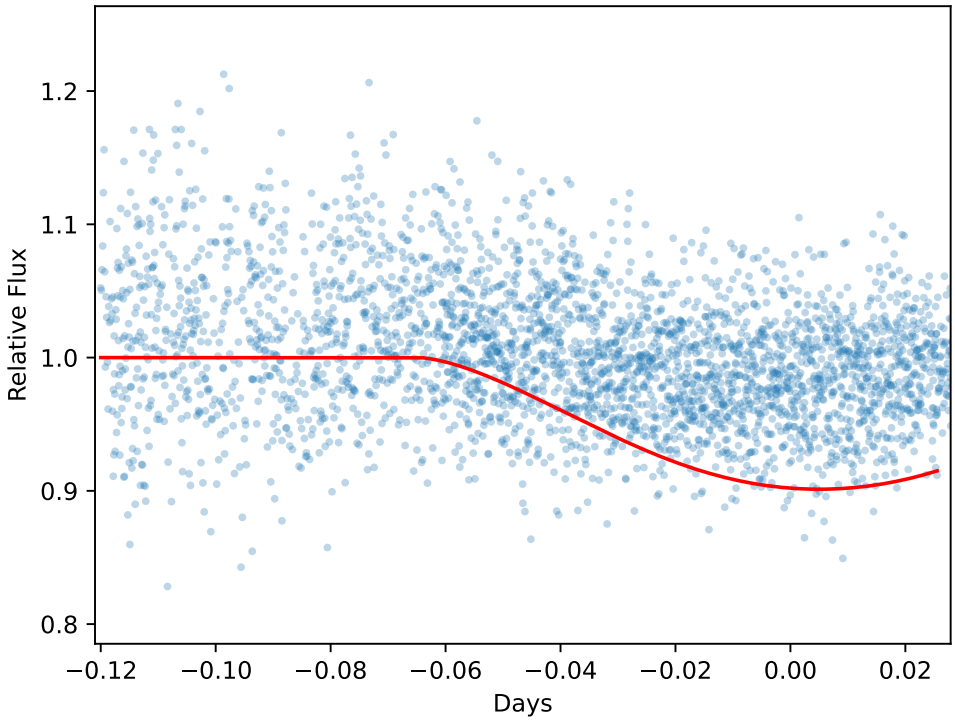

Figure 5.20: Light curve with minimum detectable injected transit injected into the raw data for HD 32715. The light curve of the model transit injected is plotted in red. Data is unbinned.

2022 Jan 18 and 2021 Oct 18 were excluded from the injection programs for HD 21844 and HD 206751 respectively to prevent the potential transits from skewing the results.

For HD 206751, the minimum injected transit detected was just 0.61 Jupiter radii. The injected transit is shown in Figure 5.21. It can be picked out via the BLS method despite some scattered points before the injection obscuring the start of the transit.

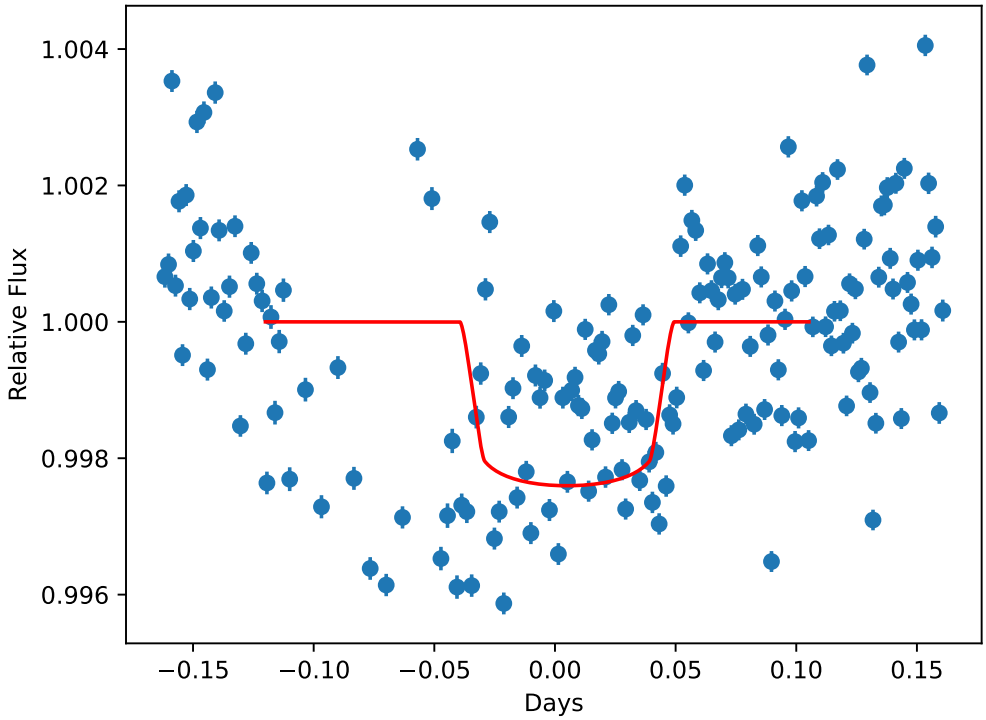

Figure 5.21: Light curve with minimum detectable injected transit injected into the raw data for HD 206751. The light curve of the model transit injected is plotted in red. Data in 40-point bins.

For HD 21844, the injected transit requires quite a bit larger radius to reach a detection at the arbitrary point in the data where the injection occurs. The resulting minimum detectable injection displayed in Figure 5.22 is 2.2 Jupiter

radii. Like for HD 32715, the BLS program is attempting to fold non-transiting data over the injected transit location because the raw data is highly scattered at the injection point. This early version of the injection program simply injects the transit to the first night of observation. To get a more complete picture, the transit must be injected at many points in the light curve to obtain a percentage of transit detected at a given radius rather than relying on a single injection at one point.

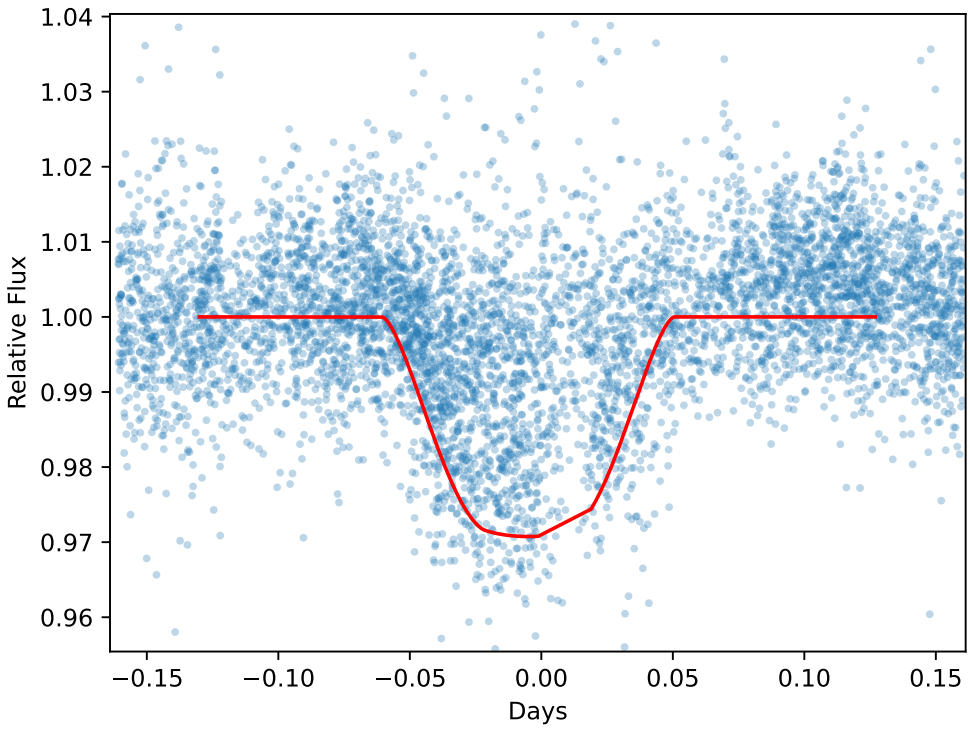

Figure 5.22: Light curve with minimum detectable injected transit injected into the raw data for HD 21844. The light curve of the model transit injected is plotted in red. Data unbinned.

With HD 206751 and HD 21844, the two stars with the most constant light curves, and excluding the days previously specified where potential transits were identified, I ran phase variable minimal detectable radius planet program. The

result is displayed in Figures 5.23 and 5.24. Figures 5.23 uses the star to planet radius ratio as a metric for the injection and Figure 5.24 has the x-axis converted to Jupiter radii using the estimated radius of the star based on the effective temperature (Equation 3.6).

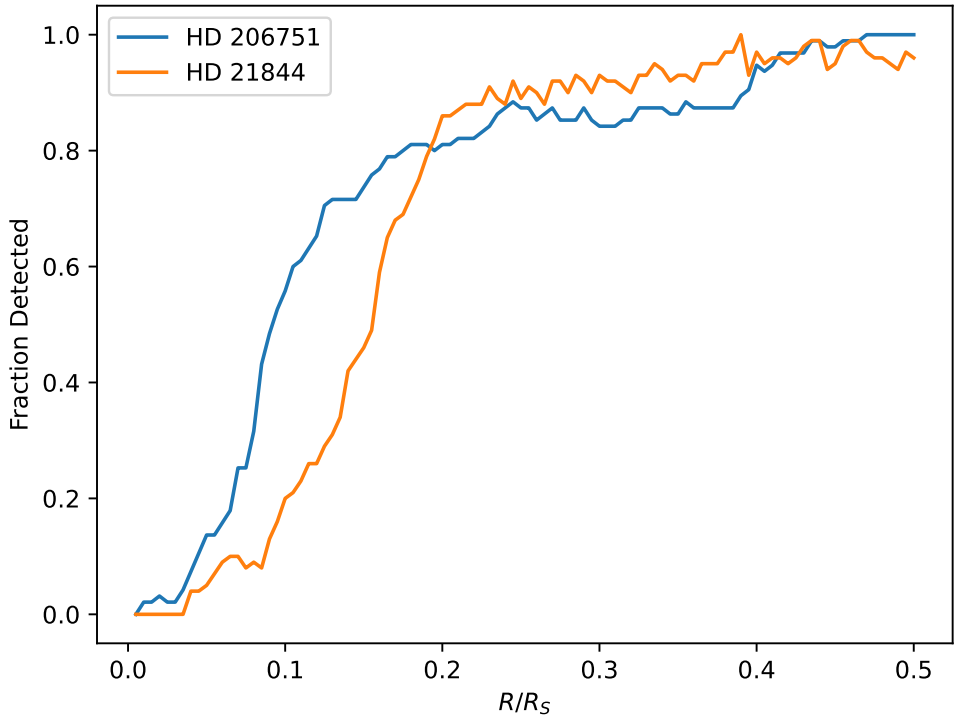

Figure 5.23: Percent of planets detected for each injected planet-to-star radius ratio

Figures 5.23 and 5.24 appear identical but there is a small horizontal scaling difference because the two stars are slightly different temperatures and therefore have different estimated radii. Both detection probability curves have a rapidly increasing section followed by a plateau where increasing the radius does not increase the detection efficiency by a significant amount. The detection probability curve for HD 206751 has more of a concave down structure in the rapid growth stage of the transit detection stage compared to HD 21844 which is concave up.

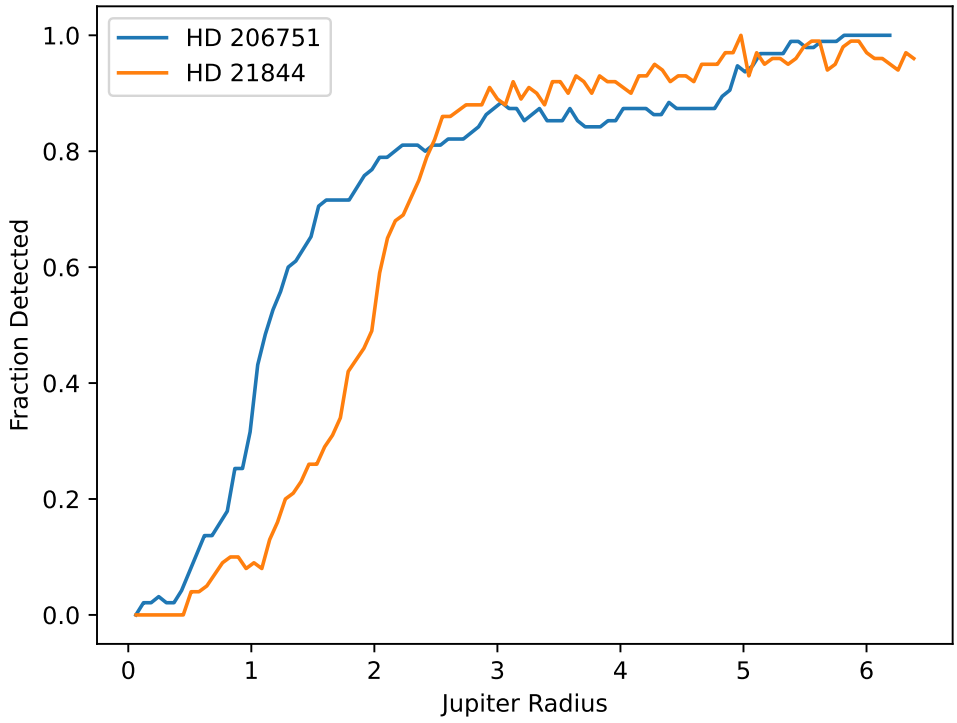

Figure 5.24: Percent of planets detected for each injected planet size

This means detections of 1 to 2 Jupiter radius planets are more likely for HD 206751.

Unlike when the minimum detectable radius was injected in a single spot, we see there is some probability that planets smaller than 2.2 Jupiter radius can be detected for HD 21844. This means the potential transit on 2022 Jan 25 is not ruled out. For HD 206751, the minimum detectable radius of 0.61 Jupiter radius is shown to be a low probability when shifting the phase of the injection. Injecting the transit in that single spot just happened to produce a sensitive detection despite injections at other phases resulting in mostly non-detections. For this reason, the transit modeled in Section 5.5 that resulted in a 6.7 Earth radius (0.598 Jupiter radius) planet is unlikely. The high degree of uncertainty in the transit depth model also supports a non-detection.

5.7 Detection Probability

Using the observation times of each of my targets, I ran the probability program described in Section 4.5.1. The result is displayed in Figure 5.25. As expected, the target with the most observations (see Table 5.2), HD 6314, has the highest likelihood for transit detections across most periods. HD 21844 only has slightly less probability of a planetary transit detection at a given period, as it was observed for 24 hours less than HD 6314. The two targets with the lowest probability of observing a transit are HD 206751 and HD 32715. HD 206751 was observed for 10 hours less than HD 21844 and HD 32715 for 13 hours less than HD 206751.

Table 5.3 summarizes the probability trends displayed in Figure 5.25. We see that both HD 21844 and HD 6314 observations have ruled out the existence of a

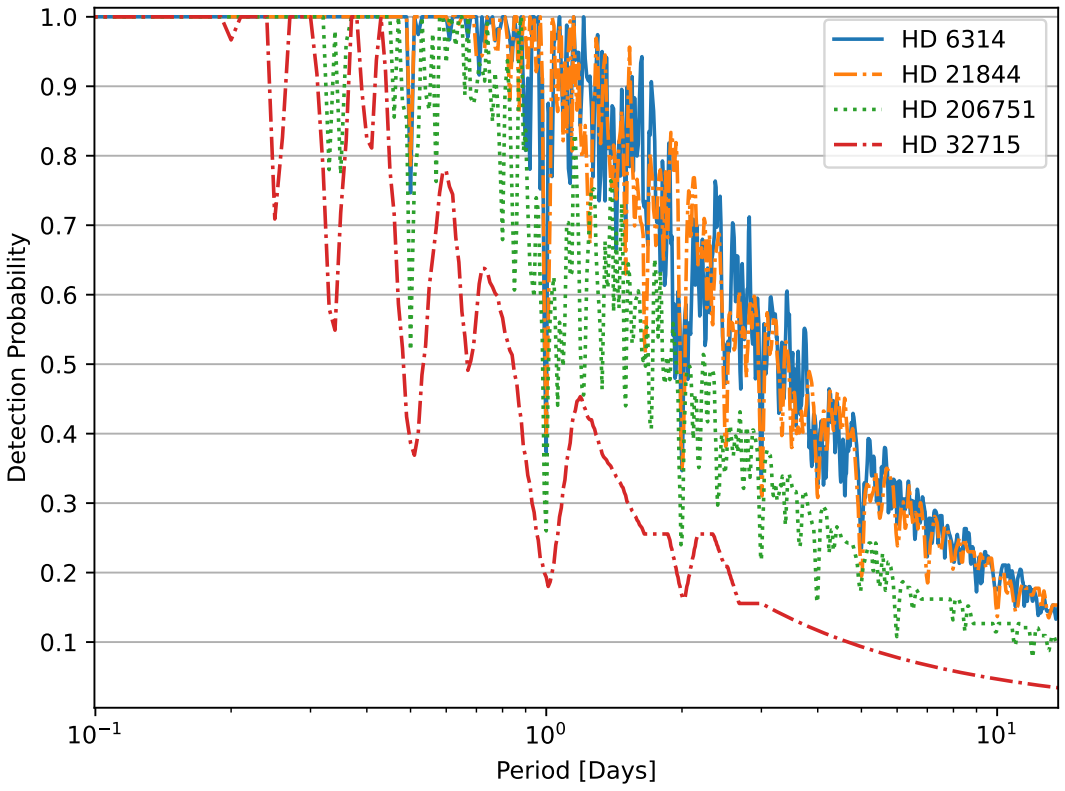

Figure 5.25: Probability of capturing a planetary transit of a given period based on the times of observation for each target.

detectable exoplanet with a period of less than half a day. An interesting trend is the diminishing returns of observing targets for longer. HD 6314 and HD 21844 were both observed for over 30 hours but HD 6314 for a day longer. However, HD 6314 only has a 1.7% increased median probability of detecting a planet with under a two-week period. HD 206751 and HD 32715 were observed for a shorter amount of time, but just observing HD 206751 for 13 hours longer than the 11 hours spent on HD 32715 increased the median probability of observing a transit of a less than two-week-period planet by 9.5%. This result means detecting a short-period planet is more likely when observing many targets for a shorter period of time rather than observing fewer targets for a long period of time. After each target receives at least 24 hours of observation, observations of old targets can resume, enhancing the probability of detecting longer period planets.

Name	**Median Prob.**	$\leq P$ **Ruled Out**	**Max** P **Ruled Out**
HD 32715	0.0666	0.20	0.43
HD 206751	0.162	0.33	0.88
HD 6314	0.278	0.50	1.21
HD 21844	0.261	0.50	1.15

Table 5.3: The last three columns of this table display for each target (1) the median probability that a transiting planet with a period of up to two weeks would be observed, (2) the period at which planets with periods less than or equal to this value are ruled out and (3) the max period which has been ruled out but some periods less than this value are not.

Chapter 6

Conclusion

6.1 Significance of Detection

A detection of a planet around a bright hot star would allow us to categorize the planetary system in better detail, giving us insight into the unique radiation environment of early-type stars. For atmospheric characterization, brighter host stars allow spectroscopic observations of a transiting planet to pick out spectral features with a higher SNR. This means the potential for detection of weak spectral features like those produced by helium and N_2 (Burrows 2014). Helium serves as an important measure for atmospheric escape as its spectral signatures can be used to determine the ultraviolet flux from a host star that is affecting the upper atmosphere (Fossati et al. 2022). To date, the hottest star that hosts a planet with a helium detection is HAT-P-32 which has an effective temperature of 6,269 K (Fossati et al. 2022). A bright star will make transmission spectra through an exoplanet atmosphere easier to detect. A helium detection around hotter stars would expand the sample radiation environments with characterized exoplanet atmospheric escape.

While this survey is most sensitive to larger-sized planets, the discovery of one planet could increase the probability of other planets existing. If a discovery of a transiting planet is made, other planets aligned with the orbital inclination of the

first detection can be discovered via the transit method. For cool Jupiters with periods $\gtrapprox$ 1 year, Zhu & Wu (2018) calculate a 96% probability that a super-Earth also exists in the system. Hot Jupiters are rarer than cold Jupiters and are less likely to host terrestrial planets orbiting interior (Zhu & Wu 2018). Since the time spent on each target is small, hot Jupiters will be detected more easily but single transits of Jupiter-sized planets warrant further observations because of the potential of capturing a second transit and the potential existence of interior planets.

6.2 Future of Exoplanet Discoveries

6.2.1 *Transiting Exoplanet Survey Satellite*

The *Transiting Exoplanet Survey Satellite* (*TESS*) mission will lead to an unprecedented discovery of new exoplanets in every corner of the night sky. The *TESS* mission, outlined in Ricker et al. (2015), will survey over 200,000 main sequence stars up to a year in length. *TESS* has the potential to make discoveries for some of the brightest stars in the night sky, "10 to 100 times brighter than those surveyed by the pioneering Kepler mission" (Ricker et al. 2015). While *TESS* is optimized to expose for dim stars, saturated bright stars can still be analyzed to derive transit curves because of how the CCD is designed. When a star in *TESS* is saturated, the pixel counts bleed over to neighboring pixels. Photometric apertures whose shape captures these pixels can produce accurate light curves. The saturation limit of *TESS* is expected to have a magnitude around 7.5 but by summing the excess pixel values for saturated stars we expect accurate photometry limited to around magnitude 4 stars to avoid charge bleeding past the size of the CCD (Ricker et al. 2015).

While this process will require additional procedures to fit an aperture to the unique shape of these saturated targets, *TESS* has the potential to discover many planets around bright stars. These planets will be able to be analyzed in incredible detail both through the precise light curves obtained by *TESS* and the follow-up observations that can benefit from the enhanced signal because of the stars' brightness. In particular, Ricker et al. (2015) optimized the survey for finding targets that can be observed with the *James Webb Space Telescope* (*JWST*) by observing stars in the ecliptic poles for longer. To date, there have been no *TESS* confirmed exoplanets within our early bright sample but 99 candidates within the sample (Akeson et al. 2013).

6.2.2 *James Webb Space Telescope*

JWST will categorize exoplanet atmospheres in unprecedented detail. It will be able to find Earth-like atmospheric features including H_2O, CO_2, O_3, CH_4 and HNO_3 by observing transmission spectra (Fortenbach & Dressing 2020). Helium signatures described in 6.1 will be more easily detected and categorized. Analysis by Allart et al. (2018) determined the helium signatures for HAT-P-11b can be detected with higher spatial and spectroscopic resolution and better precision, allowing the planetary and stellar signatures to be separated. *JWST* will be able to observe bright targets with the NIRSpec spectrometer configured in Bright Object Time Series mode down to a J-magnitude lower limit between 6.5 and 4.5 (Ferruit et al. 2014).

6.2.3 Astrometry

Astrometry uses patterns present in the proper motion of stars to identify exoplanets that perturb the star's path. Astrometry relies on precise measurements of the positions of stars rather than the flux of the stars. This means astrometry has the potential to detect smaller planets that would otherwise produce too small a transit depth to be detected or too far from the host star to have frequent transits. The radial velocity technique works more effectively for massive planets orbiting close to their host star.

With astrometry, further orbits produce easier to detect astrometric signals and the method is more sensitive to smaller planets (Lawson et al. 2004). Small planets with long orbits are greatly underrepresented in the sample of exoplanets discovered. Analysis from Lawson et al. (2004) for the later canceled NASA Space Interferometry Mission found that astrometry had the potential to discover Earth-like planets in the habitable zone and longer period Uranus and Neptune like planets with greater effectiveness than other methods of planet detection. Figure 6.1 displays mass and semi-major axis detection limits of astrometry compared to radial velocity, microlensing and transit surveys.

Astrometry can work just as effectively with bright stars as long as the position of the star can be accurately determined. The biggest astrometry survey underway is part of the *Gaia* space telescope mission. Even for saturated stars, modeling of the saturation behavior allows a centroid position to be determined (Gaia Collaboration et al. 2016). This method yields good detection efficiency for stars with $G_{\mathrm{mag}} \sim 3$ (Gaia Collaboration et al. 2016).

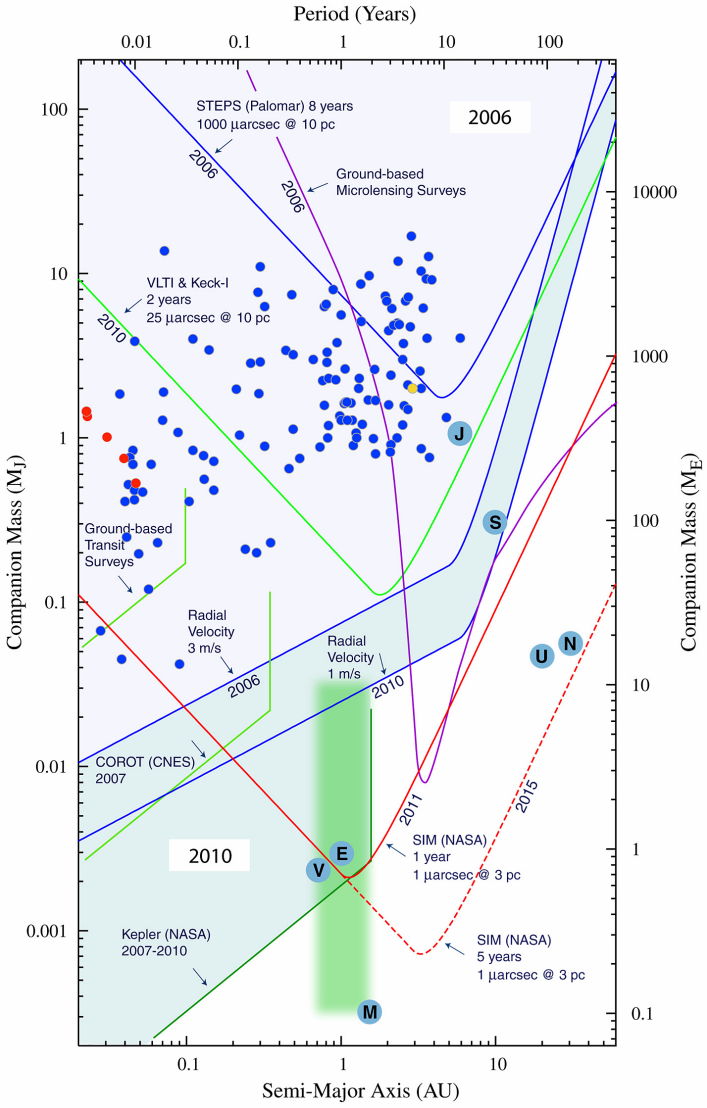

Figure 6.1: Figure from Lawson et al. (2004): "Limiting sensitivity of techniques of planet finding. Shown in the above figure are the sensitivity limits of radial velocity surveys, astrometric surveys, microlensing surveys, and space-based transit techniques. The lines show 5-σ limits with 50 re-samples. The shaded areas show the expected progress towards the detection of Earth-like planets by 2006 and 2010. Planets in our Solar System are also indicated, as well as the highlighted target area of TPF science. The filled circles indicate the planets found by radial velocity surveys (blue), transit surveys (red), and microlensing surveys (yellow). The discovered extrasolar planets shown in this plot represent the reported findings up until August 31, 2004" (Lawson et al. 2004).

6.3 Future Work

Through these pilot observations, we have demonstrated that we have the ability to detect Jupiter-sized planets around these bright hot targets using the PlaneWave 24-inch telescope. With the data that has been processed so far, we have found potential transits. We have also observed an extremely variable star and obtained a light curve that is ripe for further analysis to understand the source of variability and potentially categorize the other star in the system. We have developed a suite of packages to process and analyze light curve data. Even without detections, we have developed a method for ruling out transiting planets through simulation and injection.

Examining the data collected, we see that observing more targets for longer will dramatically increase the probability of a detection. Longer observing sessions would mean the potential partial transits observed could have been captured as full transits, greatly improving our ability to confirm the presence of a planet or see that the full shape is inconsistent with a transit. From a purely probabilistic point of view, observing for longer will allow us to rule out more transits and find longer-period planets.

The key to improving data collection efficiency is the full automation of the telescope. The telescope is in the final stages of achieving this objective. Once a reliable weather station is installed at Van Vleck Observatory, ACP can run Scheduler, a program built into ACP which executes observing plans based on targets meeting set conditions. Without the constraint of human telescope operators, data can be collected for as long as a target has a low enough airmass and the weather is favorable.

A product of the early bright star survey is the progress we made in getting

the new 24-inch PlaneWave telescope fully operational and working out every hardware and software issue that arose. At weekly telescope meetings with Dr. Roy Kilgard, Dr. Seth Redfield and Kyle McGregor, we went through each issue we encountered and worked through solutions. To date, the telescope can be controlled remotely by running simple ACP scripts. The last stage to enable full automation is the installation of the weather station.

The preliminary results of the Wesleyan early bright star survey have demonstrated the feasibility of the project and established a data reduction, analysis, probability and sensitivity infrastructure to find transits, assess their feasibility and rule out transiting planets. With more observations, the probability of making a detection will increase steadily. With the development of the programs needed to analyze the transiting data and the continued automation of the telescope, this transit search can be easily maintained with the main efforts focused on analyzing astrophysical phenomena from new exoplanets to brown dwarfs, eclipsing binaries and variable stars.

The technical insight gained from running this transit survey will enable future Wesleyan researchers to operate the telescope to conduct their own research projects. With full automation, the telescope can acquire full nights of data for multiple projects. The PlaneWave 24-inch telescope has only just begun its life as a powerful scientific instrument that will unlock new discoveries and explore other worlds.

Bibliography

Akeson, R. L., et al. 2013, PASP, 125, 989

Albrecht, S. H., Marcussen, M. L., Winn, J. N., Dawson, R. I., & Knudstrup, E. 2021, ApJ, 916, L1

Allart, R., et al. 2018, Science, 362, 1384

Astropy Collaboration et al. 2018, AJ, 156, 123

Ballard, S., et al. 2011, ApJ, 743, 200

Beaulieu, J. P., et al. 2006, Nature, 439, 437

Borucki, W. J., et al. 2010, Science, 327, 977

Boué, G., Montalto, M., Boisse, I., Oshagh, M., & Santos, N. C. 2013, A&A, 550, A53

Burke, C. J., & McCullough, P. R. 2014, The Astrophysical Journal, 792, 79

Burrows, A. S. 2014, Proceedings of the National Academy of Science, 111, 12601

Cassan, A., et al. 2012, Nature, 481, 167

Catelan, M., & Smith, H. A. 2015, Pulsating Stars

Charbonneau, D., et al. 2009, Nature, 462, 891

Chromey, F. R. 2016, To Measure the Sky

Collins, K. A., Kielkopf, J. F., Stassun, K. G., & Hessman, F. V. 2017, AJ, 153, 77

Demircan, O., & Kahraman, G. 1991, Ap&SS, 181, 313

Duric, N. 2004, Advanced astrophysics

Ferruit, P., Birkmann, S., Böker, T., Sirianni, M., Giardino, G., de Marchi, G., Alves de Oliveira, C., & Dorner, B. 2014, in Society of Photo-Optical Instrumentation Engineers (SPIE) Conference Series, Vol. 9143, Space Telescopes and Instrumentation 2014: Optical, Infrared, and Millimeter Wave, ed. J. Oschmann, Jacobus M., M. Clampin, G. G. Fazio, & H. A. MacEwen, 91430A

Fortenbach, C. D., & Dressing, C. D. 2020, PASP, 132, 054501

Fossati, L., et al. 2022, A&A, 658, A136

Fukui, A., et al. 2016, ApJ, 819, 27

Gaia Collaboration et al. 2016, A&A, 595, A1

Gänsicke, B. T., Schreiber, M. R., Toloza, O., Gentile Fusillo, N. P., Koester, D., & Manser, C. J. 2019, Nature, 576, 61

Giampapa, M. S., & Rosner, R. 1984, ApJ, 286, L19

Gillon, M., et al. 2017, Nature, 542, 456

Greivenkamp, J. E. 2004, Field guide to geometrical optics, Vol. 1 (SPIE press Bellingham, Washington)

Habets, G. M. H. J., & Heintze, J. R. W. 1981, A&AS, 46, 193

Huber, K. F., Czesla, S., & Schmitt, J. H. M. M. 2017, A&A, 597, A113

Kervella, P., Arenou, F., Mignard, F., & Thévenin, F. 2019, A&A, 623, A72

Kochanek, C. S., et al. 2017, PASP, 129, 104502

Kreidberg, L. 2015, PASP, 127, 1161

Krisciunas, K. 1993, in American Astronomical Society Meeting Abstracts, Vol. 183, American Astronomical Society Meeting Abstracts, 84.02

Lawson, P. R., Unwin, S. C., & Beichman, C. 2004, Precursor science for the terrestrial planet finder, Tech. rep., Pasadena, CA: Jet Propulsion Laboratory, National Aeronautics and Space ...

LeBlanc, F. 2010, An Introduction to Stellar Astrophysics

Lee, U., & Osaki, Y. 1982, PASJ, 34, 39

Léger, A., et al. 2009, A&A, 506, 287

Macintosh, B., et al. 2015, Science, 350, 64

Madhusudhan, N. 2019, ARA&A, 57, 617

Madhusudhan, N., Lee, K. K. M., & Mousis, O. 2012, ApJ, 759, L40

Mayor, M., & Queloz, D. 1995, Nature, 378, 355

McNally, D. 1965, The Observatory, 85, 166

Merline, W. J., & Howell, S. B. 1995, Experimental Astronomy, 6, 163

Nutzman, P., & Charbonneau, D. 2008, PASP, 120, 317

Osborn, J., Föhring, D., Dhillon, V. S., & Wilson, R. W. 2015, Monthly Notices of the Royal Astronomical Society, 452, 1707

Pecaut, M. J., & Mamajek, E. E. 2013, ApJS, 208, 9

Poro, A., et al. 2021, PASP, 133, 084201

Ricker, G. R., et al. 2015, Journal of Astronomical Telescopes, Instruments, and Systems, 1, 014003

Rodgers, A. W. 1957, MNRAS, 117, 85

Royer, F., Zorec, J., & Gómez, A. E. 2007, A&A, 463, 671

Schmidt, T. O. B., et al. 2016, A&A, 593, A75

Seach, J. M., Marsden, S. C., Carter, B. D., Neiner, C., Folsom, C. P., Mengel, M. W., Oksala, M. E., & Buysschaert, B. 2020, MNRAS, 494, 5682

Stevens, D. J., & Gaudi, B. S. 2013, PASP, 125, 933

Tassoul, J.-L. 2000, Stellar Rotation

Thompson, S. E., et al. 2016, Kepler Data Release 25 Notes, Kepler Science Document KSCI-19065-002, id.3. Edited by Jon Jenkins and Michael R. Haas

Villanueva, S., Eastman, J. D., Gaudi, B. S., Pogge, R. W., Stassun, K. G., Trueblood, M., & Trueblood, P. 2016, in Society of Photo-Optical Instrumentation Engineers (SPIE) Conference Series, Vol. 9906, Ground-based and Airborne Telescopes VI, ed. H. J. Hall, R. Gilmozzi, & H. K. Marshall, 99062L

Virtanen, P., et al. 2020, Nature Methods, 17, 261

Weber, E. J., & Davis, Leverett, J. 1967, ApJ, 148, 217

Welsh, W. F., Orosz, J. A., Carter, J. A., & Fabrycky, D. C. 2014, in Formation, Detection, and Characterization of Extrasolar Habitable Planets, ed. N. Haghighipour, Vol. 293, 125–132

Wenger, M., et al. 2000, A&AS, 143, 9

Winn, J. N. 2010, arXiv e-prints, arXiv:1001.2010

Wolszczan, A., & Frail, D. A. 1992, Nature, 355, 145

Young, A. T. 1981, Appl. Opt., 20, 533

Yu, X., Moses, J. I., Fortney, J. J., & Zhang, X. 2021, ApJ, 914, 38

Zhu, W., & Wu, Y. 2018, The Astronomical Journal, 156, 92